

G. Relevant modeling at MRI and JMA

G-1. Numerical Atmospheric Transport and Dispersion Models¹

Numerical atmospheric transport dispersion and deposition models (ATDMs) are capable of simulating air and ground surface contamination with radioactive materials from nuclear accidents. Given the time and place of emission sources, ATDMs calculate the advection, diffusion, and dry and wet deposition processes of radioactive materials. Many ATDMs are driven by meteorological parameters provided by numerical weather prediction (NWP) models. They range from high-resolution limited-area models to low-resolution global models, depending on their purposes and the available computational resources.

Although predictions by ATDMs are very informative, they have some uncertainty, which results from limited information about emission sources and incomplete model representation of transport and deposition processes, in addition to the uncertainty of NWP products. In general, the products of ATDMs should not be used for quantitative comparison with some threshold densities of radioactive materials for evacuation, but they are suitable for assessing the worst case scenario.

Although ATDMs were not used for mitigating risks of radiation exposure in the case of the accident at the Fukushima Dai-ichi Nuclear Power Plant (Iwasaki, 2013), a working group of the Meteorological Society of Japan has pointed out some ways in which numerical predictions of the atmospheric dispersion of accidentally released radioactive materials can be utilized (WGMSJ, 2014). In particular, ATDMs may be useful along with monitoring data in the following environmental emergencies:

(i) Radioactive materials floating near the ground surface:

People become internally exposed to floating radioactive materials through inhalation. For example, radioactive iodine tends to concentrate in the thyroid gland, where it may cause thyroid cancer. ATDMs are expected to provide information about contaminated air near the ground surface.

(ii) Radioactive materials deposited on the ground:

Airborne radioactive materials contaminate the ground surface through dry and wet deposition. Wet deposition, in which falling raindrops gather radioactive materials between the clouds and the ground, can cause severe radioactive contamination of the ground even far away from the emission source. Unfortunately, the performance of ATDMs in simulating wet deposition processes is not satisfactory because of NWP errors in predicting precipitation, together with the errors arising from the ATDM itself, degrade the quality of wet deposition predictions. However, ATDMs can be used to estimate the vertically integrated amount of airborne radioactive materials, which is the maximum potential wet deposition.

¹ T. Iwasaki

G-2. WMO emergency response activities and operational atmospheric transport modelling at JMA¹

G-2-1. Introduction

The Japan Meteorological Agency (JMA) was designated by the World Meteorological Organization (WMO) as a Regional Specialized Meteorological Centre (RSMC) for Atmospheric Transport Modelling (ATM) for radiological Environmental Emergency Response (EER). RSMCs-ATM are responsible for providing ATM products in response to requests by the International Atomic Energy Agency (IAEA) and members of WMO. This section briefly describes the WMO EER service and the operational atmospheric transport model used by JMA.

Table G-2-1. List of current WMO RSMCs-ATM for radiological EER.

	Organization (country)	Start year	WMO Regional Association
RSMC Tokyo	Japan Meteorological Agency (Japan)	1997	WMO Regional Association II (Asia)
RSMC Beijing	Chinese Meteorological Administration (China)	1997	
RSMC Obninsk	Roshydromet* (Russia)	1997	
RSMC Montréal	Canadian Meteorological Center (Canada)	1989	WMO Regional Associations III and IV (South, Central, and North America, and the Caribbean)
RSMC Washington	National Environmental Prediction Center (USA)	1993	
RSMC Melbourne	Bureau of Meteorology (Australia)	1995	WMO Regional Association V (South-West Pacific)
RSMC Exeter	UK Met Office (UK)	1989	WMO Regional Associations I and VI (Africa and Europe)
RSMC Toulouse	Meteo France (France)	1989	

* The Russian Federal Service for Hydrometeorology and Environmental Monitoring

G-2-2. WMO RSMCs-ATM

After the Chernobyl nuclear power plant accident in April 1986, the Commission for Basic Systems (CBS) of WMO held a series of discussions and decided to launch an ATM EER service to meet the broad interest in the atmospheric dispersion of toxic radiological materials. The national meteorological and hydrological services of the United Kingdom, France, and Canada started their ATM services in 1989. Table G-2-1 lists the current RSMCs-ATM. JMA was designated an RSMC at the 49th session of the WMO executive council in 1997 and initiated its service on 1 July 1997. Two other RSMCs (Beijing and Obninsk) in Regional Association (RA) II (Asia) also began operation then. The German Weather Service (Deutscher Wetterdienst) has been contributing by acting as the WMO Regional Telecommunications Hub (RTH) for EER. In this role, it receives nuclear and radiological emergency messages from IAEA and disseminates early warning messages through the WMO Global Telecommunication System (GTS).

Each RSMC is responsible for providing forecasts within its region of responsibility (see Table G-2-1). RSMCs provide their ATM products not only to IAEA but also to WMO members within their

¹ M. Sakamoto

region of responsibility. For example, if a WMO member in RA II asks for support, RSMCs Tokyo, Beijing, and Obninsk serve this request. If RSMC Tokyo receives a request from a WMO member in RA V (South-West Pacific), which is adjacent to RA II and includes part of Southeast Asia, RSMC Tokyo replies to the member and forwards the request to RSMC Melbourne, the responsible center of RA V, which services the request.

More than one RSMC is allocated to each RA so that RSMCs can compare and evaluate the accuracy of their products before presenting a concise statement of ATM forecast results and the meteorological situation within the region. In the case of RA V, where there is only one center, RSMCs Montréal and Washington provide services in support of RSMC Melbourne.

G-2-3. International coordination by the CBS expert team

CBS formed an expert team to organize emergency responses and related activities, and the team is currently called the Expert Team on Emergency Response Activities. This team, which is composed of representatives from the RSMCs, RTH, WMO, and IAEA secretariats and other related international organizations, meets once every two years to discuss issues regarding ATM services at related WMO centers.

The team reports to the CBS Open Programme Area Group on Data-Processing and Forecasting System, which then conveys the contribution through CBS to the WMO Executive Council and the World Meteorological Congress. For instance, the issues and activities discussed at the team meeting in Vienna in 2011 were contributed to CBS-15 in Jakarta in 2012 and the 65th Executive Council meeting in 2013.

G-2-4. Standard EER products

The standard set of EER products, as defined in Appendix II-7 of the Manual on the Global Data-processing and Forecasting System (WMO, 2010), consists of seven charts (Fig. G-2-1) and a joint statement on weather and atmospheric dispersion forecasts within the region.

(a) Trajectory chart (Fig. G-2-1 (a))

Trajectories of three tracers released at 500, 1500, and 3000 m above the surface are shown in the chart. The tracers are released at the start release time of radioactive material and move with the wind stream, without considering disturbance by atmospheric diffusion and viscosity. The forecast extends to 72 hours after the forecast initial time. Changes in the height of each tracer with time are shown below the map in the figure.

(b) Time-integrated concentration charts (Fig. G-2-2 (b))

The 24 hour time-integration concentration of the radioactive material by 24, 48, and 72 hours after the forecast initial time are presented in three charts. The distributions shown in Fig. G-2-2 (b) is the average from the surface to an altitude of 500 m. The unit of radioactivity in the charts is $\text{Bq s} / \text{m}^3$, and indicates the number of radiological decays in the 24 hour period per cubic meter of atmosphere.

(c) Total deposition charts (Fig. G-2-3 (c))

The distribution of radioactive materials that have accumulated through dry and wet deposition processes on the surface from the initial release time is shown in three charts, for 24, 48, and 72 hours after the forecast initial time. The unit of deposition is Bq / m^2 , which is the number of radiological decays per second per square meter of surface.

(d) Joint Statement

A concise consensual plain text description of weather conditions and the atmospheric dispersion forecast of the radioactive material is prepared by the RSMCs within each region. For example, RSMCs Tokyo, Beijing, and Obninsk prepare this statement whenever documentation for RA II is needed. The statement basically includes a synopsis of the current situation and the forecast of meteorological conditions in the area of concern, along with the transport modelling results, including the differences and similarities among the models.

The impact of an accident depends not only on the amount of radioactive material released but also on the types of radionuclides and on the exposure pathway. The products produced by the WMO RSMCs consist only of weather forecast and atmospheric transport information; they do not address the consequences of the release of toxic materials in the region. Therefore, expertise in nuclear science and in biology, including knowledge of the characteristics of nuclear decay and the impact of radiation exposure on the bodies of humans and animals, is needed to interpret any impacts from the products.

WMO RSMCs present their ATM products to IAEA and the registered organizations of WMO member states. The ATM results should be analyzed by specialized international organizations such as IAEA and WHO, and by relevant national governmental organizations of the influenced member states.

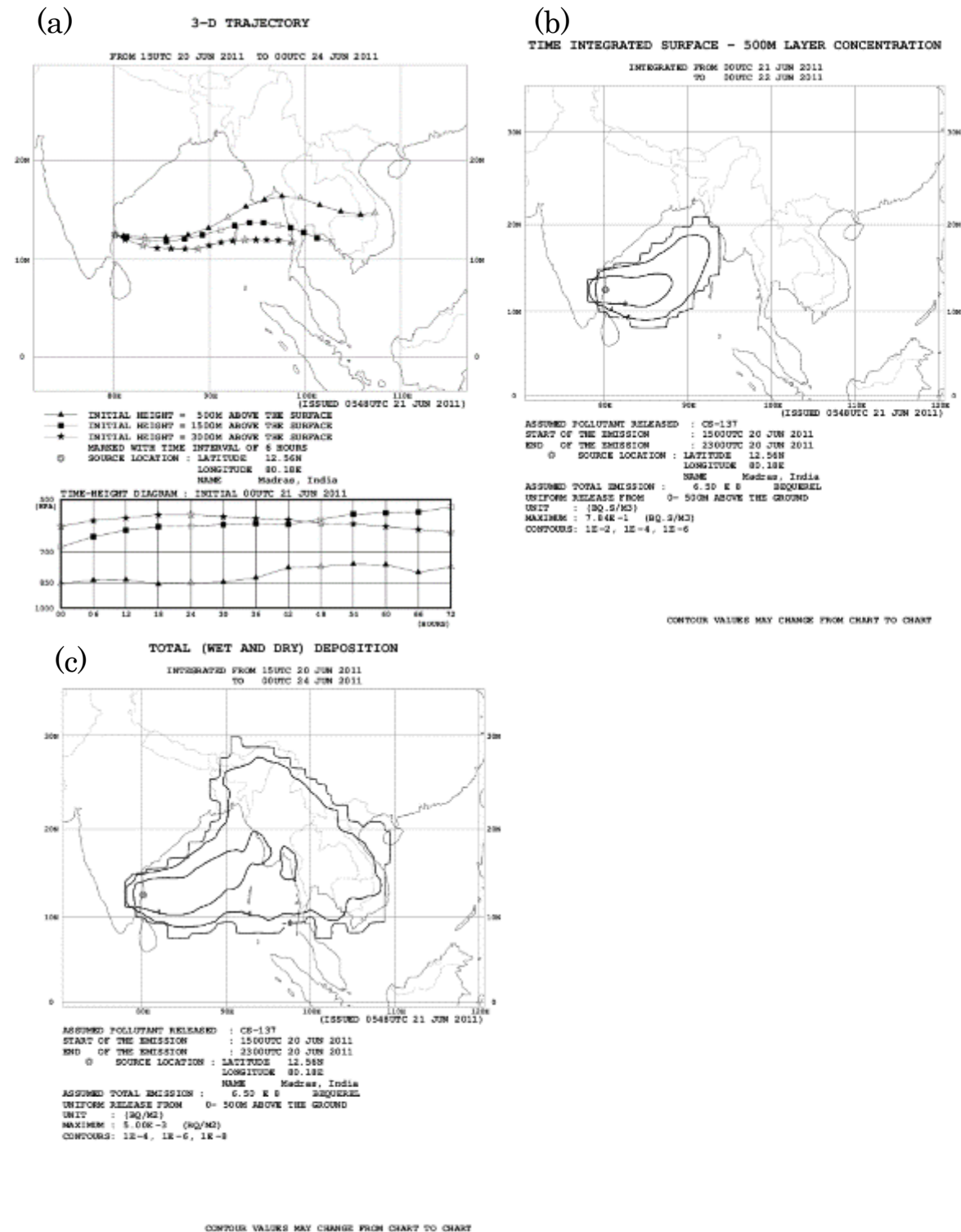


Fig. G-2-1. Examples of the standard EER products: (a) trajectory chart and time–height diagram for the three tracers, (b) time-integrated concentration chart, (c) total deposition chart.

G-2-5. JMA's ATM for EER

The atmospheric transport model for EER by JMA uses a Lagrangian approach in which many tracer particles are released at the time and location of the pollutant emissions and the model simulates the displacement of the tracers. The tracers move by advection and diffusion, and they may descend and settle onto the surface through dry or wet deposition. Table G-2-2 shows the specifications of the atmospheric transport model. The effects of advection, diffusion and deposition are simulated by using 3-hourly grid point values from JMA's operational global numerical weather prediction. Tracer particles are also removed by nuclear decay. Iwasaki et al. (1998) described the development of the ATM and the results of an international comparison experiment, and Sakamoto (2013) gave a detailed description of the model.

Lagrangian ATMs have the advantage that they conserve the total amount of released tracers. There is neither a fictitious loss nor a gain if the treatment of deposition and of radiological decay is appropriate. Almost all RSMCs² use Lagrangian atmospheric transport models.

Table G-2-2. Specifications of the ATM for the radiological EER at RSMC Tokyo.

Type of ATM	Lagrangian
Vertical diffusion scheme	Louis et al. (1982)
Dry deposition scheme	Kitada et al. (1986)
Wet deposition scheme	Kitada (1994)
Number of tracer particles	100,000
Horizontal grid cell size for concentration and deposition	1° × 1°
Weather forecast system	JMA's Operational Global Forecast (TL959L60 Global Spectral Model)*
Grid point data used in the ATM	Lower Resolution (TL319L40) Grid Point Data prepared for ATM. The ATM uses gridded wind velocity, precipitation, specific humidity, temperature, surface pressure, and horizontal pressure gradient data.

* When the start release time is earlier than the forecast initial time, the operational global analysis data are also used as for the period before the forecast initial time.

G-2-6. A case study of a wildfire event

To demonstrate the performance of JMA's ATM for EER, a case study of a wildfire event, during which the distributions of the tracers were optically observed by a satellite imager, is presented in this subsection.

According to the fire and smoke products produced by the Office of Satellite and Product Operations of the U.S. National Environmental Satellite, Data, and Information Service (NESDIS), on 28 April 2011 wildfires were started by lightning around the Okefenokee National Wildlife Refuge (ONWR) in Georgia, USA. The fires continued for months, and smoke was clearly observed, especially during the period from 19 to 23 June. Visible and infrared images acquired by the MODIS instrument on the AQUA satellite were published on the NESDIS website. Although there were other wildfires during the same period, the large wildfires around ONWR produced the most smoke.

In the visible image acquired by the AVHRR sensor on NOAA-18 at 17:00 UTC on 23 June (Fig. G-2-2a), a broad thick band of clouds covers parts of the central and eastern United States and southern Canada, but there is little cloud cover over the western Atlantic Ocean at around 30°N. In the

² The only exception is the ATM of RSMC Toulouse, which uses an Eulerian approach.

differential infrared image acquired at the same time (Fig. G-2-2b), the broad gray area spreading over the Atlantic from the U.S. east coast was identified as smoke released by the ONWR wildfires. Because emittance of infrared (IR) radiation of smoke is heavily dependent on the wavelengths, a differential IR image is used to reveal the presence of the smoke.

Figure G-2-3 shows the result of the ATM forecast, in which tracers are uniformly released from the surface in the ONWR from 00:00 UTC on 15 June to 00:00 UTC on 23 June 2011. To simulate the broad distribution for the long forecast period, the number of the tracers was set to be two million. The distribution of the total column amount of tracers at 00:00 UTC on 23 June in the forecast results, presented using a log-scale in Fig. G-2-3, generally corresponds to the area of smoke shown in Fig. G-2-2b. Few tracers are below the thick cloud area seen in Fig. G-2-2a because the considerable amount of precipitation predicted by the global forecast washed out the tracers. In fact, NESDIS reported that there was no smoke identified north of Virginia because of heavy rain. A thick area of tracers also extends from the northeastern Labrador-Ungava Peninsula to the north Atlantic. JMA's global analyses of geopotential height at 500 hPa and wind distribution at 700 hPa at 00:00 UTC on 23 June 2011 (Fig. G-2-4) show a cutoff low pressure system around Newfoundland. The tracers over the Labrador-Ungava Peninsula followed the counterclockwise air circulation around this low, and their distribution corresponds well to the smoke distribution in Fig. G-2-2b. The tracers were relatively high because of upwelling flow around the low.

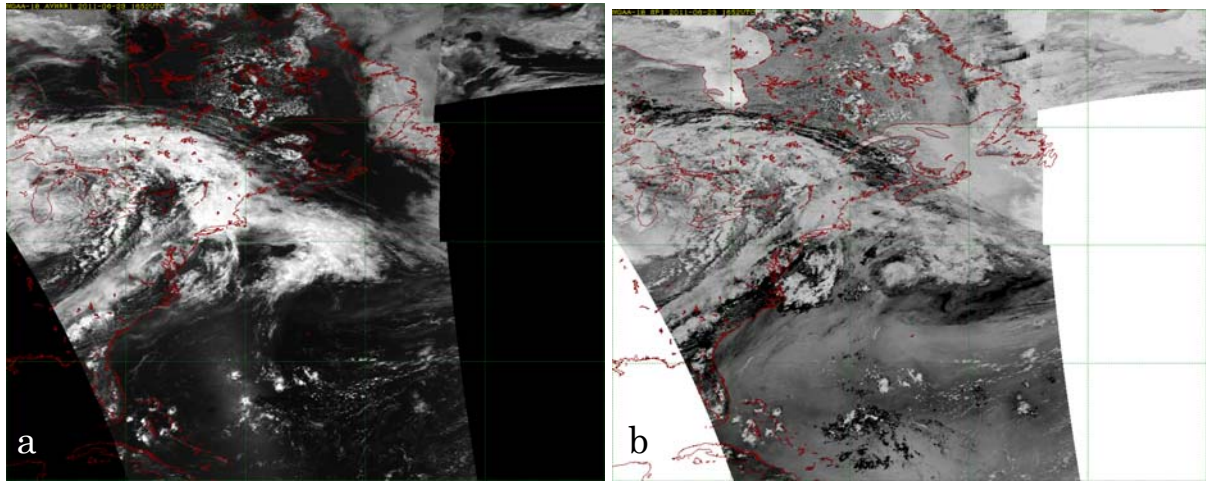


Fig. G-2-2. Images acquired by NOAA-18 / AVHRR at 17:00 UTC on 23 June 2011: (a) visible image, (b) differential infrared image.

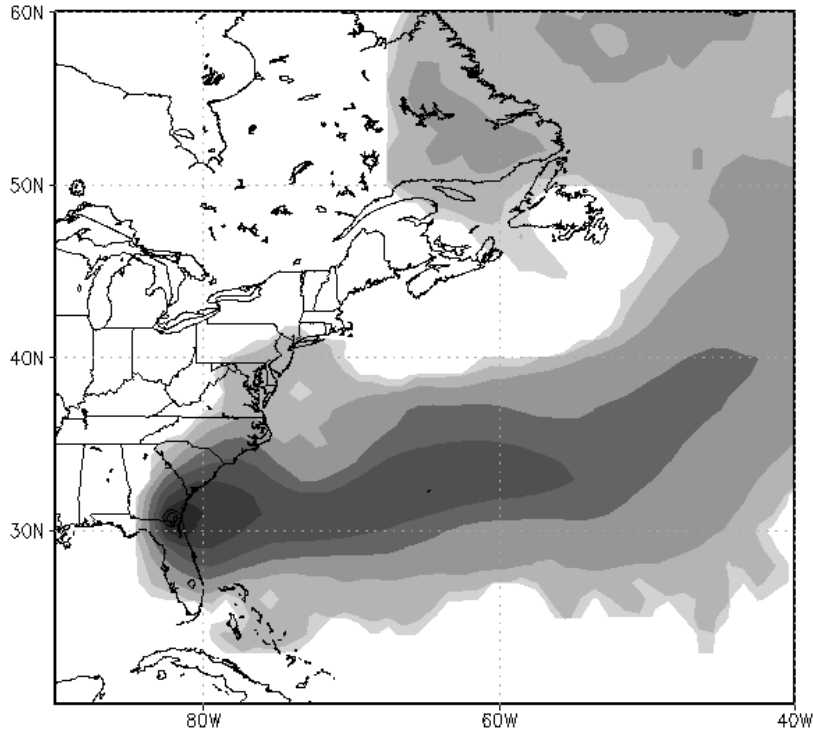


Fig. G-2-3. Distribution of the total column amount of tracers in the ATM forecast for 00:00 UTC on 23 June 2011.

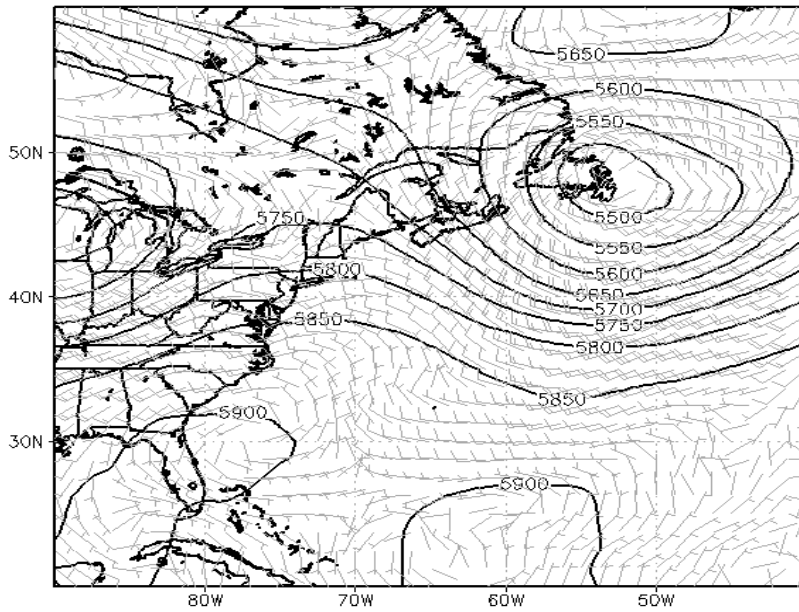


Fig. G-2-4. Analysis of the geopotential height at the 500 hPa level (contour interval, 50 m), and wind barbs at 700 hPa at 00:00 UTC on 23 June 2011.

G-3. NHM-Chem: Sensitivity of Cs deposition to the size and hygroscopicity of Cs-bearing aerosols¹

G-3-1. Abstract

The emission, transport, and deposition of ¹³⁷Cs released by the Fukushima Daiichi Nuclear Power Plant (FDNPP) accident were simulated with consideration of the microphysical properties (i.e. size and hygroscopicity) of the Cs-bearing aerosols (carrier aerosols of radioactive Cs). The sensitivity of the simulated deposition of ¹³⁷Cs to the size and hygroscopicity of the carrier aerosols was assessed and compared with the sensitivity to meteorological fields simulated using different dynamics and physics modules. Two types of Cs-bearing aerosols were considered in the simulation, supermicron water-insoluble and submicron water-soluble particles, in accordance with previously published observational evidence (Adachi et al., 2013 and Kaneyasu et al., 2012). Even though the same transport model was used, the simulated depositions were very different when meteorological models with different dynamics and physics modules were used. The sensitivity of ¹³⁷Cs deposition to the carrier aerosol size and hygroscopicity, in which the proportion of water-insoluble aerosol emission ranged from 10% to 90%, during the early stage ranged from March. 11-12 to Mar. 12-20, was found to be lower but still as important as the sensitivity to meteorological fields simulated using different dynamics and physics modules. To better understand the environmental behavior of the radioactive Cs discharged from the FDNPP, knowledge of the carrier aerosol microphysical properties is as important as the accuracy of the meteorological simulation and the emission scenario.

G-3-2. Introduction

Three months after the FDNPP accident, Chino et al. (2011) estimated the emission amounts of radioactive ¹³⁷Cs and ¹³¹I associated with the accident by using a reverse estimation method in which both the environment monitoring data and an atmospheric dispersion simulation were used (see section D-2). Since then, many modeling studies have been conducted to assess the emission, dispersion, and deposition amounts of radionuclides associated with the accident (Morino et al. 2011; Yasunari et al., 2011; Schöppner et al. 2011; Takemura et al., 2011; Sugiyama et al., 2012; Stohl et al., 2012; Terada et al., 2012; Katata et al., 2012a, 2012b; Morino et al., 2013; Adachi et al., 2013; Hu et al., 2014; Katata et al., 2015; Sekiyama et al., 2015).

Because numerical models use uncertain parameters and rough assumptions, model inter-comparison and intra-comparison (or sensitivity) studies are essential to assess the uncertainties of numerical simulations. In fact, previous model inter-comparison studies have shown that simulation results vary substantially among models (Draxler et al., 2013a; Katata et al., 2015; SCJ, 2014). Although model inter-comparison studies can show how the simulation results of models using different dynamics, physics, and chemistry modules and emission scenarios differ overall, the reasons for the differences cannot be easily identified. In contrast, model intra-comparison (or sensitivity)

¹ M. Kajino

studies can identify the modules or parameters that are responsible for different results, but under limited conditions that the simulations are performed only by a single model.

Morino et al. (2013) investigated the sensitivity of radioactive Cs dispersion and deposition to the wet-scavenging modules and emission scenarios. Like most previous studies, for the meteorological field they used the output of only one meteorology model. In this study, we used several different meteorology models and simulation techniques to evaluate sensitivity of the transport model results to different meteorological simulations as well.

Another important aspect of this study is that we examined the sensitivity of the simulated deposition to the microphysical properties of Cs-carrying aerosols for the first time. Adachi et al. (2013) reported that in the early stage of the accident, the carrier aerosols of radioactive Cs were spherical, water-insoluble particles (hereafter, Cs-balls), and they predicted that the atmospheric behavior of these aerosols would be different from that of the submicron water-soluble particles described by Kaneyasu et al. (2012). Washout (or below-cloud scavenging) of aerosol particles (i.e., of both types described in this paragraph) is not usually efficient because of their small inertia and slow Brownian motion. In contrast, the submicron water-soluble particles are efficiently scavenged via rainout (or in-cloud scavenging) because the Kelvin (curvature) effect is enough small. Washout is probably the dominant scavenging process of water-insoluble aerosols, because very high supersaturation conditions are needed for rainout of water-insoluble aerosols to occur.

The purpose of this study was to assess the sensitivities described above in order to evaluate the uncertainties of the simulated deposition of ^{137}Cs caused by aerosol microphysical properties (i.e., aerosol size and hygroscopicity) and to compare it to the uncertainty caused by the use of different meteorological simulations.

G-3-3. NHM-Chem

NHM-Chem is a chemical transport model, offline- or online-coupled with Japan Meteorological Agency's non-hydrostatic model (JMA-NHM; Saito et al., 2007). NHM is a numerical weather prediction model of JMA. An Eulerian regional chemical transport model, Regional Air Quality Model 2 (RAQM2) (Kajino et al., 2012a), is used to simulate emission, transport, and deposition of trace gases and aerosols. RAQM2 implements a triple-moment modal aerosol microphysics module that assumes a log-normal size distribution of aerosol populations. This model describes the nature of aerosol dynamical processes, such as nucleation, condensation, coagulation, hygroscopic growth, dry deposition, grid-scale rainout (cloud condensation and ice nuclei activation and subsequent mixed-phase cloud microphysical processes) and washout (coagulation between aerosols and settling hydrometeors) processes, and sub-grid-scale convection and scavenging processes. In the study, the offline-coupled NHM-Chem was used in order to use different meteorological models alternatively, such as the Weather Research and Forecasting (WRF) model (Skamarock et al., 2008) to drive RAQM2.

G-3-4. Simulation settings

In this study, meteorology simulations were performed with NHM and WRF with two different cloud microphysics modules, Morrison et al. (2009) and Lim and Hong (2010), referred to as WRF-MORR and WRF-WDM6, respectively. The two WRF simulations were used so that the sensitivity to just the cloud microphysical process (grid-scale) could be assessed, because wet deposition of ^{137}Cs over Japan dominated over dry deposition in this study.

NHM, WRF, and RAQM2 shared the same domain, which consisted of 215×259 grid cells with a 3 km horizontal resolution; this model domain is slightly larger than the area shown in Fig. G-3-1. There were 50 vertical layers up to 50 hPa in NHM, 28 layers up to 100 hPa in WRF, and 20 layers up to 10 km in RAQM2. JMA Meso-Regional Objective Analysis data sets (3 hourly, $5 \text{ km} \times 5 \text{ km}$) were used for the initial and boundary conditions of NHM and WRF. The same analysis data sets were used for the spectral nudging in NHM and for the grid nudging in WRF.

The radionuclide transport version of NHM-Chem was developed for simulations of nuclear power plant accidents such as the FDNPP accident (Adachi et al., 2013; Sekiyama et al., 2015). This version of NHM-Chem uses an aerosol dynamics module that is simplified from that described by Kajino et al. (2012a) because aerosol hygroscopicity and the particle size distribution are assumed to be constant during transport. The nature of the aerosol dynamics such as dry deposition and grid-scale rainout/washout processes are thus described on the basis of the prescribed size distribution and hygroscopicity. Details of the dry and wet deposition processes are described by Kajino et al. (2012a; their sections 2.2.7 and 2.2.8). Even aerosols that are completely water-insoluble (i.e., hygroscopicity $\kappa = 0$) can act as cloud condensation nuclei under highly supersaturated conditions. Although water-insoluble aerosols can coagulate with cloud droplets within a cloud (this is also rainout process), for simplicity, in this study we did not consider rainout of Cs-balls and only washout in their wet deposition modeling. Sub-grid scale convection and scavenging processes were not considered. The fog deposition process of Katata et al., (2015) was considered.

We used the emission scenario for ^{137}Cs discharged from the FDNPP from Terada et al. (2012), and considered Cs-bearing aerosols to be of two types. Supermicron water-insoluble particles (Cs-balls) had a lognormal size distribution, number equivalent geometric mean dry diameter $D_{\text{g,n,dry}} = 2.3 \text{ }\mu\text{m}$, geometric standard deviation $\sigma_{\text{g}} = 1.3$, particle density $\rho_{\text{p}} = 2.0 \text{ g/cm}^3$, and $\kappa = 0$ (Adachi et al., 2013), and submicron water-soluble particles (Kaneyasu et al., 2012) had a lognormal size distribution, $D_{\text{g,n,dry}} = 0.1 \text{ }\mu\text{m}$, $\sigma_{\text{g}} = 1.6$, $\rho_{\text{p}} = 1.83 \text{ g/cm}^3$, and $\kappa = 0.4$.

For the sensitivity studies, taking into consideration the findings of Adachi et al. (2013), we allowed the proportion of early-stage emissions consisting of Cs-balls during the early stage to range from 10% to 90%, and the ending date of the early stage to range from 12 to 20 March 2011.

The analysis period was from 00:00 UTC on 11 March to 00:00 UTC on 1 April, with a spin-up period of 3 days. Thus, the entire simulation period was from 8 March to 1 April 2011.

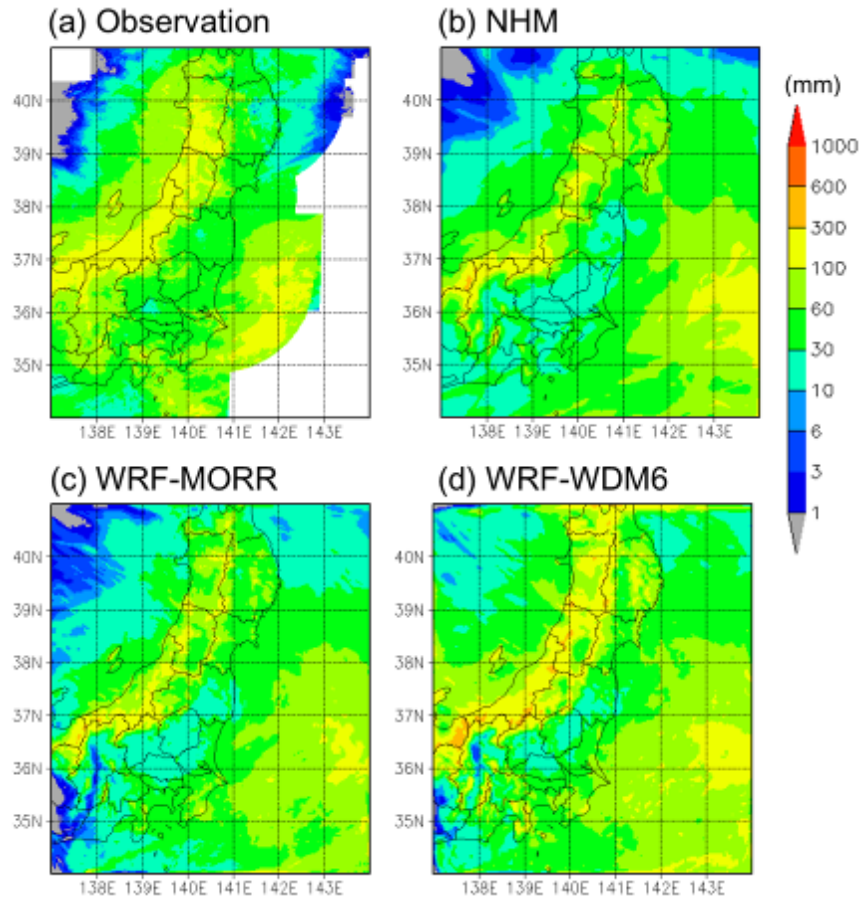


Fig. G-3-1. Cumulative precipitation (mm) from 11 March to 1 April: (a) Radar/rain gauge-analyzed precipitation (RAP) data and precipitation simulated by (b) NHM, (c) WRF-MORR, and (d) WRF-WDM6.

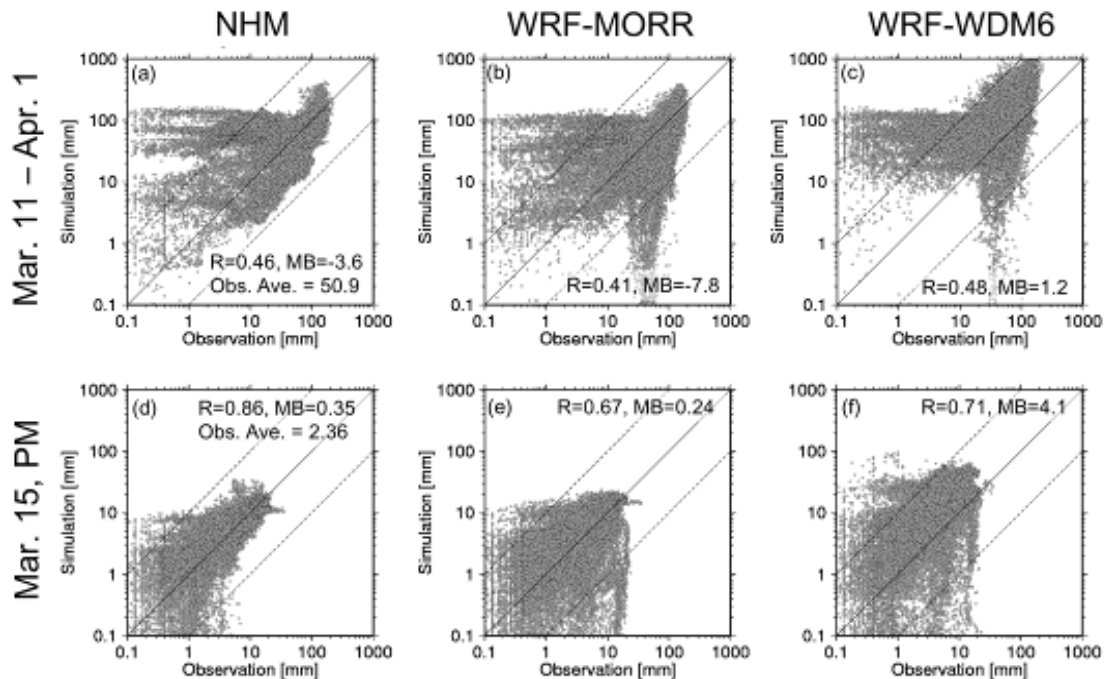


Fig. G-3-2. Scattergrams of simulated and observed (RAP) cumulative precipitation: (a–c) from 11 March to 1 April and (d–f) in the afternoon of 15 March. Simulations were by (a, d) NHM, (b, e) WRF-MORR, and (c, f) WRF-WDM6. The plotted data are for all grids for which both observation and simulation data were available. Although the data are plotted on a log-log scale, the statistics R , mean bias (MB), and the observation average (Obs. Ave.) were calculated on a linear-linear basis.

G-3-5. Results and discussion

We compared observed and simulated cumulative precipitation from 11 March to 1 April among the three meteorology models (Figs. G-3-1 and G-3-2). For observed data, we used JMA's radar/rain gauge-analyzed precipitation (RAP) data, which were interpolated to the 3 km resolution grid. We also compared observed and simulated cumulative precipitation on the afternoon of 15 March (Fig. G-3-2, lower panels), when substantial deposition occurred on land (e.g., Morino et al., 2013). All three simulations overestimated precipitation over the ocean by a factor of more than 10 (data points above the 10:1 simulation:observation line in Fig. G-3-2), and the two WRF simulations also underestimated precipitation in the southwestern part of the domain by a factor of more than 10 (data points below the 1:10 simulation:observation line in Fig. G-3-2). Our focus was on land regions where the ^{137}Cs deposition was large ($>10 \text{ kBq/m}^2$) (see Fig. G-3-3), and we did not expect the large discrepancies between the simulated and observed precipitation over the ocean to substantially affect the modeling of ^{137}Cs deposition in land areas.

The differences due to the different cloud microphysics modules were notable. The simulated precipitation spatial distribution patterns of the two WRFs were similar and different from the NHM pattern, whereas the precipitation amounts in WRF-MORR were fairly close to those in NHM, and those in WRF-WDM6 were much larger than the amounts in the other two simulations (Fig. G-3-2). WRF-WDM6 overestimated precipitation substantially over high-altitude regions (corresponding to locations where the simulated precipitation was $>600 \text{ mm}$; Fig. G-3-1d). In the afternoon of 15 March, the overestimation of WRF-WDM6 was substantial; the mean bias (MB) was 4.1 mm and the observation average was 2.36 mm. Judging from the values of the correlation coefficient (R), the performance of NHM was best among the three meteorological simulations ($R = 0.86$, $\text{MB} = 0.35 \text{ mm}$). The MB of WRF-MORR was smallest ($\text{MB} = 0.24 \text{ mm}$), but owing to the square shape of the plotted data, R was 0.67.

Comparison of cumulative ^{137}Cs deposition amounts between aircraft observations (Torii et al., 2012) and simulations by NHM, WRF-MORR, and WRF-WDM6 (Fig. G-3-3), performed under the assumption that 100% of ^{137}Cs was carried by water soluble particles, showed that NHM simulated too much deposition in northern areas (Yamagata, Miyagi, and Iwate prefectures). This deposition was caused by rainout of ice phase precipitation (snow and graupel). For accurate simulation of rainout of ^{137}Cs , the vertical distribution of the ^{137}Cs and the hydrometeor mixing ratio must be accurately predicted. However, because no observations of the vertical profiles of ^{137}Cs are available for the time period of this study, the reason for this overestimation is impossible to identify.

WRF-MORR also simulated too much deposition in Yamagata and Miyagi prefectures, but WRF-WDM6 simulated less deposition in this area. The two WRF simulations reasonably reproduced depositions in the highest deposition areas ($>1000 \text{ kBq/m}^2$), but depositions in those areas were underestimated by NHM. The two WRF simulations also reasonably reproduced the higher depositions in the mountainous regions of Tochigi and Gunma prefectures, but they overestimated depositions in the southern area (Tokyo, Kanagawa, Shizuoka, and Chiba prefectures). The NHM

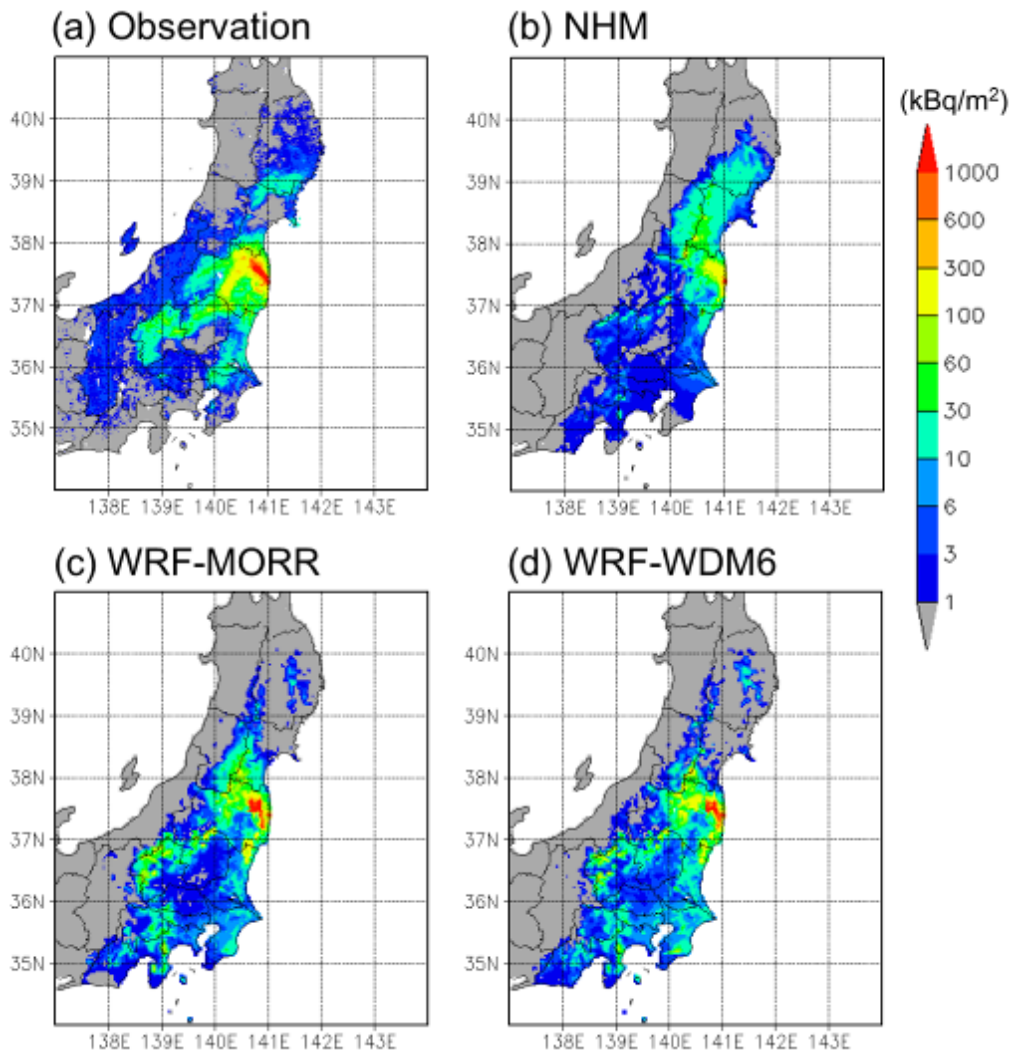


Fig. G-3-3. Cumulative ^{137}Cs deposition amounts (kBq/m^2) in (a) aircraft observations and (b) NHM, (c) WRF-MORR, and (d) WRF-WDM6 simulations. Simulated depositions are shown only for land areas to facilitate visual comparison with the observed deposition.

simulation underestimated deposition in all of these areas (i.e., in Tochigi and Gunma prefectures as well as in Tokyo, Kanagawa, Ibaraki, and Chiba prefectures). It is notable that, even though the transport model was the same, the simulated depositions varied substantially among the different meteorological simulations.

Figure G-3-4 shows depositions of water-soluble and water-insoluble particles simulated by using the three meteorological fields on both land and ocean areas. We compared the simulated depositions with aircraft observation data (Fig. G-3-3a) interpolated to the 3 km resolution grids of the models in Fig. G-3-5. Note that following Morino et al. (2013) and Katata et al. (2015), R and MB were calculated only when the observed values were larger than $10 \text{ kBq}/\text{m}^2$.

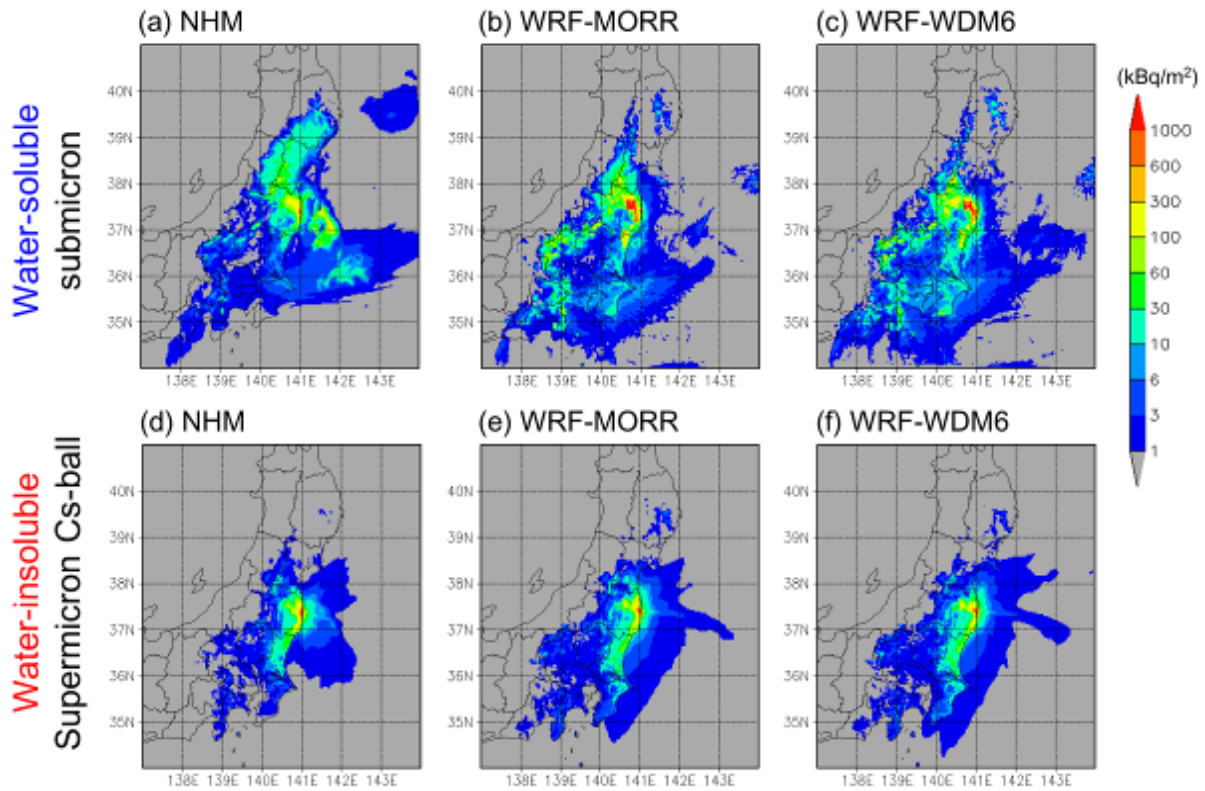


Fig. G-3-4. Cumulative depositions (kBq/m^2) simulated using the meteorological fields of (a, d) NHM, (b, e) WRF-MORR, and (c, f) WRF-WDM6 under the assumption that 100% of Cs was carried by (a–c) water soluble or (d–f) water insoluble particles.

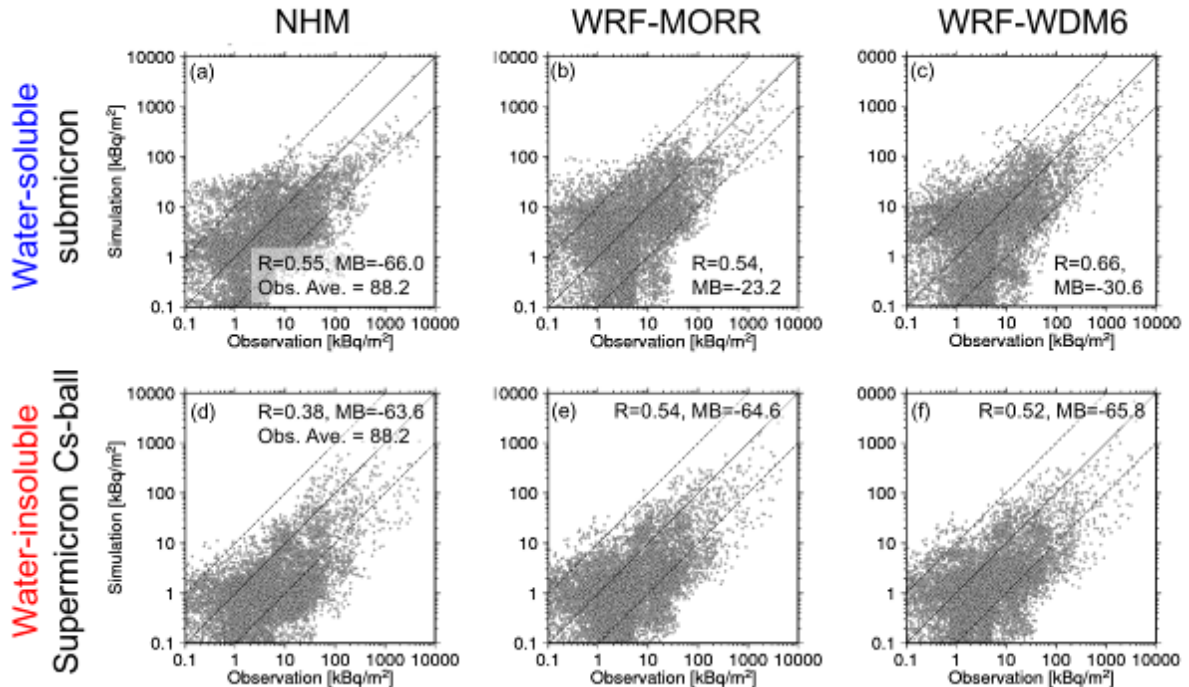


Fig. G-3-5. Scattergrams of cumulative deposition between the (a, d) NHM, (b, e) WRF-MORR, and (c, f) WRF-WDM6 simulations and aircraft observations. The simulations were performed under the assumption that 100% of Cs was carried by (a–c) water soluble or (d–f) water insoluble particles. Although the data are plotted on a log-log scale, the statistics R and mean bias (MB) were calculated on a linear-linear basis.

The simulated results were substantially different between Cs-bearing particles assumed to be 100% water soluble or water insoluble, because rainout of the Cs-balls was not considered to occur (compare upper and lower panels in Figs. G-3-4 and G-3-5), whereas the dry deposition velocity of Cs-balls was approximately four times that of the water-soluble submicron aerosols. It is interesting that although the simulation of precipitation by NHM/WRF-WDM6 was good/poor, the simulation of deposition by NHM/WRF-WDM6 was poor/good.

Adachi et al. (2013) detected Cs-balls only in samples collected during the early stage of the accident (14–15 March), but they reported that radioactive Cs was carried by water-soluble aerosols later (20–22 March). Kaneyasu et al. (2012), who analyzed samples collected from 28 April to May 12 and during 12–26 May (i.e., after the later sampling period of Adachi et al., 2013), also reported the radioactive Cs to be carried by water-soluble aerosols. Therefore, the assumption of 100% water-insoluble or water-soluble particles (Figs. G-3-4 and G-3-5) was not realistic; rather, reality must lie somewhere in between. Therefore, under the assumption that Cs-balls, as indicated by Adachi et al. (2013), were emitted only in the early stage of the accident, we used the following settings to test the sensitivity to aerosol microphysical properties:

1. We set the proportion of Cs-ball emissions to values from 10% to 90% during the early stage.
2. We started the early stage on 11 March but varied its ending date between 12 and 20 March 2011 (i.e., before the later sampling of Adachi et al., 2013).

We next compared cumulative depositions simulated using the meteorological fields calculated by NHM and the two WRF simulations between two extreme cases: 10% Cs-ball emission until 12 March and 90% Cs-ball emission until March 20 (Fig. G-3-6). The statistics (MB, root mean square error (RMSE) and *R*) of these comparisons are presented in Table G-3-1, together with the statistics for the three meteorological simulations when emissions were assumed to consist of 100% water-soluble submicron particles.

It is notable that even when the transport model settings and aerosol properties were the same, the fractional bias (MB divided by the observation average) ranged from 0.25 to 0.74, differing by approximately threefold, among the three different meteorological simulations. This difference is marked, because it means, for example, that the emission amount estimated by an inverse model from the deposition amount could vary threefold, depending on the meteorological model used. The ranges of MB, RMSE and *R* in the sensitivity to aerosol properties test results were smaller than their ranges in the sensitivity to meteorology test results (Table G-3-1), but the differences were similarly marked. The fractional bias range differed by approximately twofold between WRF-MORR and WRF-WDM6 (0.35–0.74 and 0.38–0.66, respectively). Therefore, the sensitivity of ¹³⁷Cs deposition to aerosol microphysical properties was as important as its sensitivity to the meteorological simulation used.

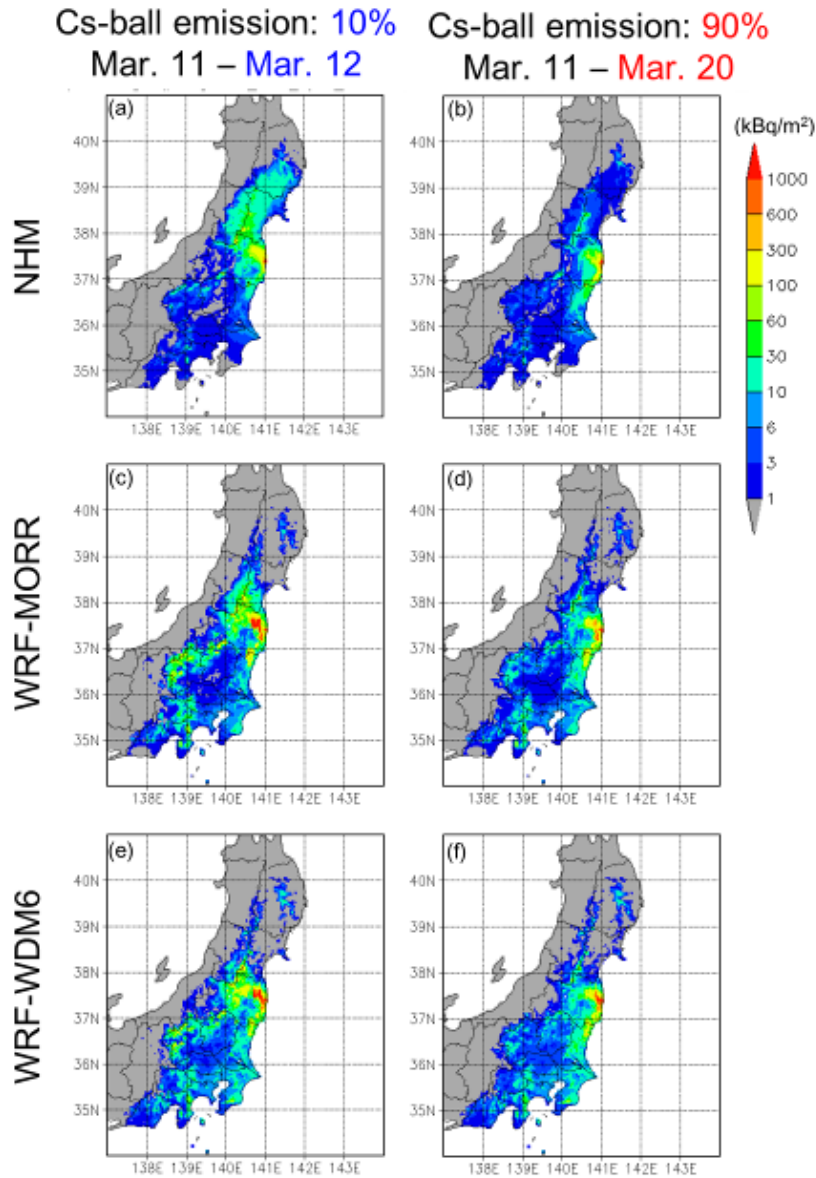


Fig. G-3-6. Simulated cumulative depositions (kBq/m^2) using the meteorological fields calculated by (a, b) NHM, (c, d) WRF-MORR, and (e, f) WRF-WDM6 between the two extreme aerosol microphysical assumptions: (a, c, e) 10% Cs-ball emission from 11 to 12 March and (b, d, f) 90% Cs-ball emission from 11 to 20 March.

Table G-3-1. Ranges of the statistics between observed and simulated cumulative depositions between the two extreme sensitivity tests (10% or 90% Cs-balls and 12 or 20 March as the ending date of the early stage) with each meteorological simulation (first to third row). The bottom row shows the same statistics among the meteorological simulations when no Cs-balls were assumed.

Sensitivity to	MB ¹	RMSE ¹	R ¹	Obs. Ave.	Simulation settings		
	(min:max)	(min:max)	(min:max)		Meteorological simulation	Cs-ball fraction	Ending date of early stage
	(kBq/m^2)	(kBq/m^2)	(-)	(kBq/m^2)			
Aerosol properties	-68.5 : -65.5	274.3 : 295.0	0.39 : 0.55	88.2	NHM	10-90%	Mar.12 - 20
Aerosol properties	-57.2 : -22.8	251.1 : 272.5	0.53 : 0.59	88.2	WRF-MORR	10-90%	Mar.12 - 20
Aerosol properties	-54.6 : -30.2	225.9 : 244.2	0.65 : 0.70	88.2	WRF-WDM6	10-90%	Mar.12 - 20
Meteorology simulations	-66.0 : -23.2	233.0 : 274.9	0.54 : 0.66	88.2	NHM, WRF-MORR, WDM6	0%	-

¹ linear-linear statistics

G-3-6. Summary

We simulated the emission, transport, and deposition of ^{137}Cs released due to the FDNPP accident. The sensitivity of the simulated depositions of radioactive Cs to the size and hygroscopicity of the carrier aerosols was assessed and compared with the sensitivity to the meteorological simulation.

Two types of Cs-bearing aerosols, water-insoluble supermicron particles (Cs-balls) and water-soluble submicron particles were considered in the simulation. The simulated depositions of the two aerosols were significantly different because rainout was not considered to occur with Cs-balls, and the dry deposition velocities of Cs-balls were approximately four times those of the water-soluble particles.

Even when the transport model was used with exactly the same settings, the simulated depositions were very different among the different meteorological simulations: The fractional bias (MB divided by observation average) ranged from 0.25 to 0.74, an approximately threefold difference. The sensitivity of ^{137}Cs deposition to particle size and hygroscopicity (determined by adjusting the proportion of water-insoluble Cs emission between 10% and 90% and the ending date of the early stage between 12 and 20 March 2011) was smaller but just as important as the sensitivity to the meteorological simulation (in which 100% of Cs was assumed to be water soluble, as in previous studies). To better understand the environmental behavior of radioactive Cs discharged from the FDNPP, knowledge of the aerosol microphysical properties is as important as the accuracy of the meteorological simulations and emission scenarios.

In future work, several new wet deposition modules and emission scenarios, together with new meteorological simulations (for example, NHM-LETKF as in Sekiyama et al., 2015), will be added to the current sensitivity analysis study to provide a more robust uncertainty estimation of the numerical simulation techniques. It would also be interesting to estimate the sensitivity to the modeling approach (Lagrangian or Eulerian), because the both approaches have been used in FDNPP accident simulation studies.

G-4. NHM-Chem-LETKF¹

G-4-1. Introduction

Generally, it is difficult to tell how high a model's resolution needs to be to simulate the atmospheric transport and deposition of radionuclides. Japan has a complex topography, and Fukushima is well known as a mountainous region. Although the Fukushima Daiichi Nuclear Power Plant (FDNPP) is located on the Pacific Ocean coastal plain, the Abukuma Mountains (up to 1000 m in elevation) are located just behind the FDNPP. Beyond the Abukuma range, Fukushima City is located in a long narrow basin, called the Naka-dori Valley, about 70 km from the FDNPP, and Mt. Azuma, a 2000-m peak, rises just behind the city. This topography is well depicted by a grid with a 500-m horizontal resolution (Fig. G-4-1c). In contrast, it is difficult to recognize these features on a grid with a 15-km horizontal resolution (Fig. G-4-1a). Most regional models used to simulate radiation from the Fukushima nuclear accident have used a 3-km horizontal resolution (Fig. G-4-1b) (e.g., Chino et al., 2011; Sugiyama et al., 2012; Morino et al., 2013; Adachi et al., 2013; Hu et al., 2014), but it is not clear that a horizontal resolution of 3 km allows the advection and deposition of radionuclides from the FDNPP accident to be properly reproduced. Furthermore, global simulation models of the FDNPP accident (e.g., Yasunari et al., 2011; Takemura et al., 2011; Schöppner et al., 2011; Stohl et al., 2012) commonly have had horizontal resolutions much lower than 15 km, too low to depict Fukushima's complex topography in detail.

In this study, we investigated whether models using a 3-km grid (the typical regional model resolution) or a 15-km grid (representative of the global model resolution) are suitable for simulating the radioactive pollution from the FDNPP accident by comparing simulation results obtained with such models with those obtained with a very high resolution model (500-m grid). We performed tests with both Eulerian and Lagrangian chemistry transport models, but both models were driven by the same meteorological analyses. However, we encountered difficulties in obtaining meteorological analyses with an arbitrary horizontal resolution; an interpolated, extrapolated, or nudged meteorological analysis is likely to be a mixture of different resolution analyses. Therefore, we conducted our own data assimilation to obtain analysis data with an arbitrary resolution, independent of any model or analysis with another resolution.

¹ T. T. Sekiyama and M. Kunii

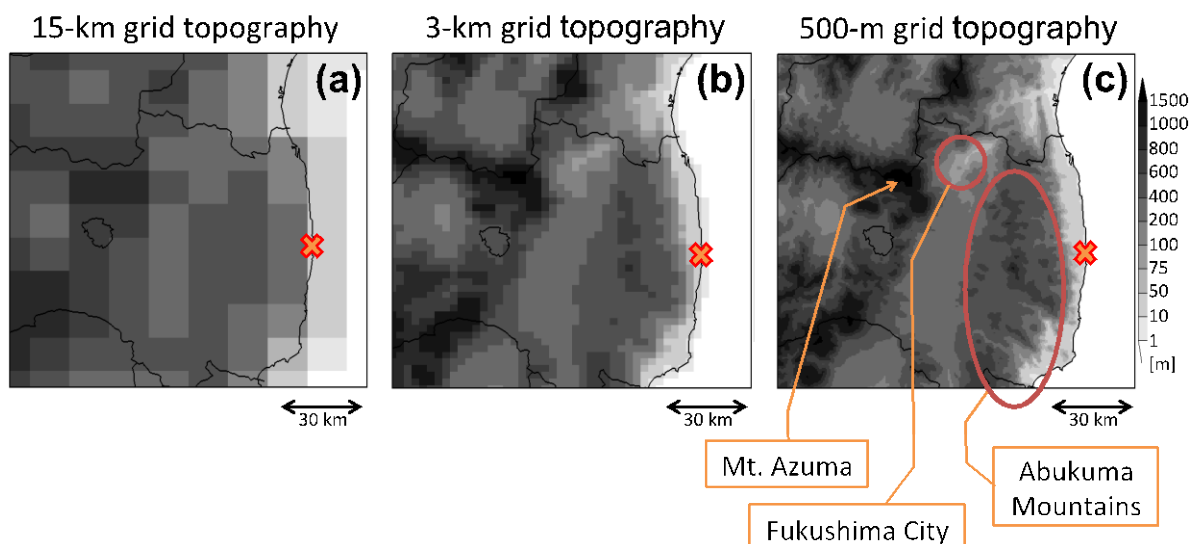


Fig. G-4-1. Fukushima topography depicted at three different scales: (a) 15-km grid, (b) 3-km grid, and (c) 500-m grid. The cross mark indicates the location of FDNPP. The Abukuma Mountains are up to about 1000 m high, and Fukushima City is located in a narrow basin 70 m above sea level (asl). The highest of the several peaks of Mt. Azuma is 2035 m asl.

G-4-2. Model Description

Before performing the radionuclide transport calculations, we prepared meteorological analyses with three different horizontal resolutions by using a flow-dependent data assimilation system assembled and validated by Kunii (2013). This data assimilation system consists of the Japan Meteorological Agency's nonhydrostatic model (JMA-NHM; Saito et al., 2006, 2007) and a local ensemble transform Kalman filter (LETKF; Hunt et al., 2007) called NHM-LETKF. The system calculated all of the necessary meteorological variables, which were stored after every 10 minutes of simulation time and used subsequently to drive the radionuclide transport models. In this study, the horizontal resolutions were set to 15 km, 3 km, and 500 m. A one-way nested data assimilation scheme was implemented, in which the first guess of a lower resolution model was used for the boundary conditions for the integration with a finer resolution model (cf. Kunii, 2013). Each nested inner model ran independently of the outer coarse-resolution model except for the boundary conditions. Operationally, JMA-NHM is initialized by the JMA non-hydrostatic model four-dimensional variational data assimilation system (JNoVA, Honda et al., 2005; see also section C-8). Most regional simulation models used in Japan and some models used by the World Meteorological Organization Task team for the FDNPP accident use JNoVA grid-point-value (GPV) data as initial/boundary conditions or pseudo-observations (e.g., Chino et al., 2011; Morino et al., 2013; Adachi et al., 2013; Draxler et al., 2013a; Saito et al., 2015). In contrast, we calculated our meteorological analyses using our own data assimilation system (NHM-LETKF) instead of JNoVA GPV data.

The 15-km-grid analysis was calculated by the outermost NHM-LETKF; its domain covered East Asia and it consisted of 20 ensemble members. The initial and boundary conditions of the NHM-LETKF cycle were obtained from the JMA operational global prediction system. The covariance localization parameters were set to 150 km in the horizontal, 0.2 natural-logarithmic

pressure-coordinate in the vertical, and 3 hours in time. As observation data for assimilation, we used JMA's operational dataset, which is integrated and quality-controlled for JNoVA mesoscale weather prediction, as described by Kunii (2013). The JNoVA dataset contains observations acquired by radiosondes, weather observatories, pilot balloons, wind profilers, aircraft, ships, buoys, and satellites, but satellite radiances and radar precipitation analyses were not assimilated in this study. Instead, we assimilated additional surface wind observations acquired by JMA's Automated Meteorological Data Acquisition System (AMeDAS) and Tokyo Electric Power Company's (TEPCO) monitoring posts. The TEPCO monitoring posts are located at FDNPP and at Fukushima Dai-ni Nuclear Power Plant, which is 12 km south of FDNPP.

The 3-km-grid analysis was calculated by the first nested NHM-LETKF, the domain of which covered eastern Japan. The lateral boundary conditions were supplied by the output of the outer (15-km-grid) NHM-LETKF cycle. This NHM-LETKF was implemented with almost the same configuration of JMA-NHM as the 15-km simulation, but the convective parameterization scheme was not activated. We used the same observation data (i.e., JNoVA, AMeDAS, and TEPCO datasets) as in the 15-km data assimilation. Next, the 500-m grid analysis was calculated by the second nested NHM-LETKF, the domain of which domain mostly covered most of Fukushima Prefecture. The lateral boundary conditions were supplied from the outputs of the 3-km NHM-LETKF cycle. Basically, The same configuration of the 500-m-grid JMA-NHM s were was basically implemented the same in the 500-m grid spacing JMA-NHM as that of the 3-km simulation. Again, the same observation data were assimilated during the second nested NHM-LETKF cycle.

We conducted Eulerian simulations with NHM-Chem. NHM-Chem is a meteorology model (JMA-NHM; Saito et al., 2007) coupled offline with a chemical transport model (Regional Air Quality Model 2; RAQM2) that was developed by Kajino et al. (2012a). The details of RAQM2 are described in Chapter G-3. The meteorological analyses were taken into RAQM2 every 10 minutes and linearly interpolated within that 10 minute interval. RAQM2 and NHM-LETKF shared the same model domains and horizontal grid resolutions, but their vertical resolutions were converted from NHM-LETKF's original number of layers to RAQM2's 20 layers. The combined system is called NHM-Chem-LETKF. We used the ^{137}Cs emission scenario from FDNPP estimated by the Japan Atomic Energy Agency (JAEA) (cf. Chino et al., 2011). For comparison, we also conducted Lagrangian simulations using the JMA operational Regional Atmospheric Transport Model (JMA-RATM), which was developed by Shimbori et al. (2009, 2010). The details of JMA-RATM are described in Chapter E. The meteorological analyses were taken into JMA-RATM every 1 hour. After the model calculations, the hourly concentration and deposition outputs were multiplied by the JAEA hourly ^{137}Cs emission rate.

G-4-3. Results and discussion

We focus here on the simulation of ^{137}Cs on 15 March 2011 (UTC) because we were interested in the radioactive plumes that moved landward. The standard experiment with the JAEA emission scenario performed by Morino et al. (2013) showed that most of the ^{137}Cs deposition on land (mainly in Fukushima Prefecture) occurred from 15 to 16 March (Japanese Standard Time; JST). This period accounted for 72% of the total amount deposited on land from 10 March to 20 April 2011. We found large differences among the analyses in the horizontal winds in the planetary boundary layer (PBL) (Fig. G-4-2). The 15-km analysis (Fig. G-4-2a) did not represent the northerly winds along the Naka-dori Valley around Fukushima City because the 15-km-grid model could not represent the Abukuma Mountains or the Naka-dori Valley. In the 3-km (Fig. G-4-2b) and 500-m (Fig. G-4-2c) analyses, the wind fields were roughly the same, but only the 500-m analysis reproduced the fine wind structure over the mountains and valleys.

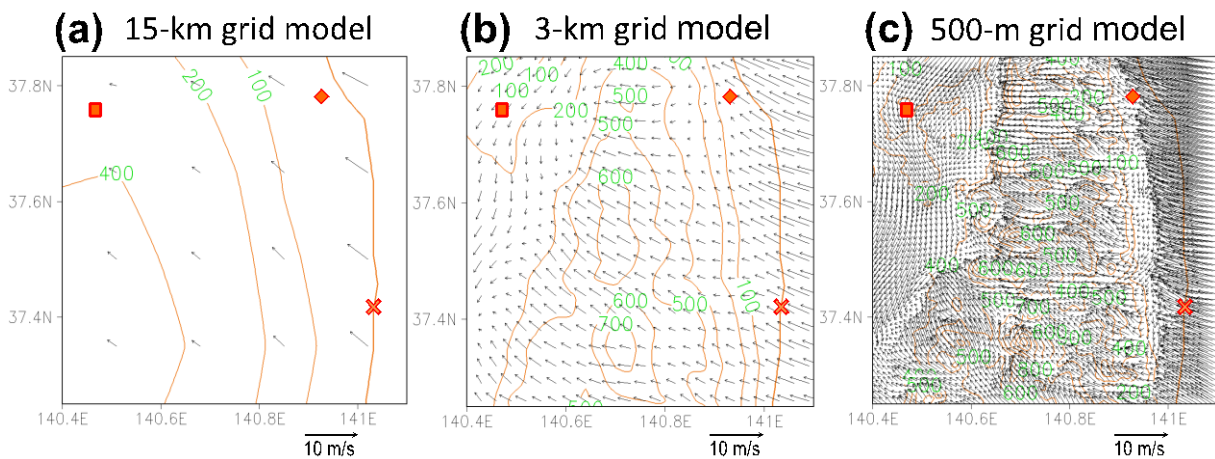


Fig. G-4-2. Lowest model level (20 m above ground level) wind direction and speed (10-minute mean) in the northern Abukuma Mountain area, Fukushima Prefecture, at 15:00 UTC on 15 March 2011, simulated by (a) the 15-km-grid JMA-NHM, (b) the 3-km-grid JMA-NHM, and (c) the 500-m-grid JMA-NHM. The cross mark indicates the location of FDNPP, the diamond indicates the location of the AMeDAS Souma observatory, and the square indicates the location of the AMeDAS Fukushima City observatory.

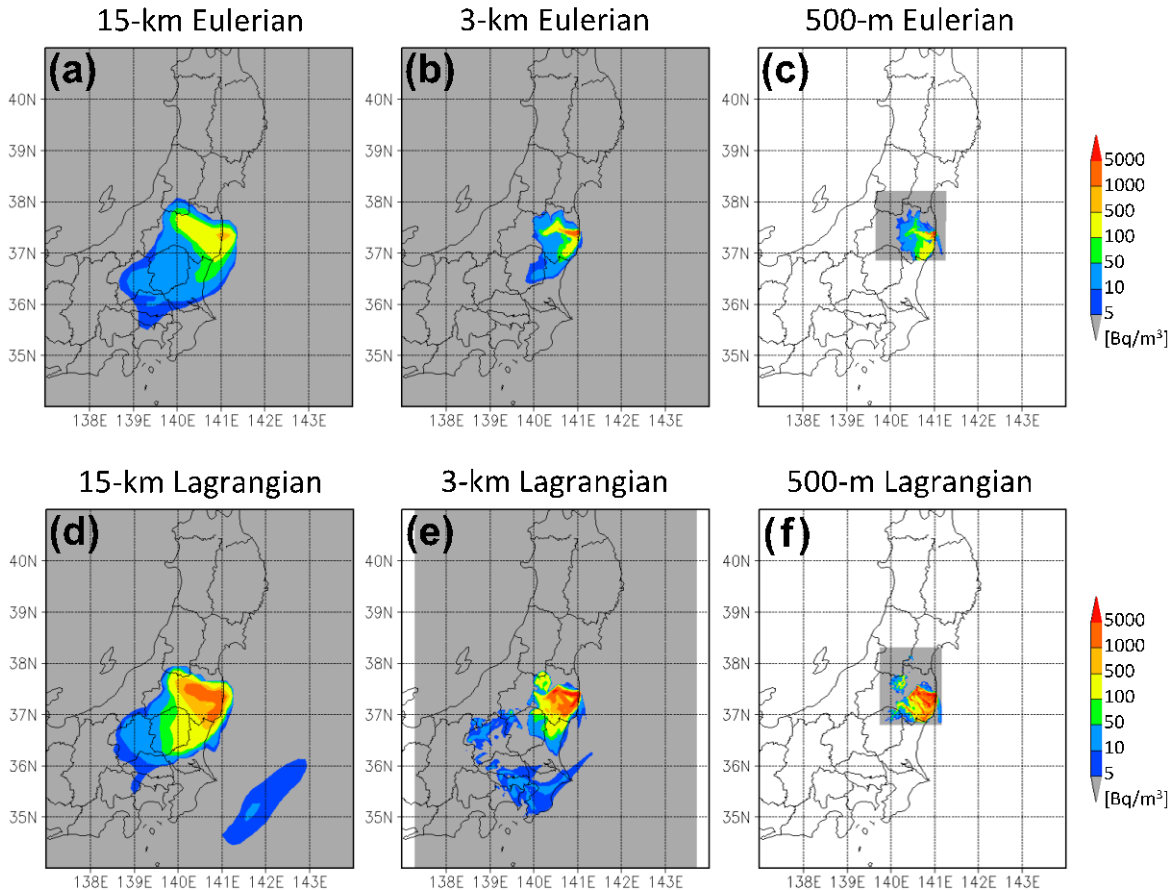


Fig. G-4-3. Surface ^{137}Cs concentrations averaged from 00:00 UTC on 15 March to 00:00 UTC on 16 March 2011 as simulated by the Eulerian model (RAQM2) using the (a) 15-km, (b) 3-km, and (c) 500-m meteorological analysis, and by the Lagrangian model (JMA-RATM) using (d) 15-km, (e) 3-km, and (f) 500-m meteorological analysis.

According to the TEPCO monitoring post data, the wind in the vicinity of FDNPP gradually changed in a clockwise direction from northerly to southeasterly between 06:00 JST (21:00 UTC the day before) and 12:00 JST (03:00 UTC) on 15 March 2011. The wind continued southeasterly for more than 10 hours, blowing inland from the coastal FDNPP site. During that time, the radioactive plume would have been carried across Fukushima and neighboring prefectures. In the Eulerian simulation results, the ^{137}Cs distributions showed good agreement between the 3-km (Fig. G-4-3b) and 500-m (Fig. G-4-3c) simulations. The ^{137}Cs plume crossed over the Abukuma Mountains but was mostly blocked by Mt. Azuma and other mountains west of the Naka-dori Valley. However, the 15-km Eulerian simulation (Fig. G-4-3a) could not represent this blockage of the ^{137}Cs plume, which spread broadly through the Naka-dori Valley as far as Yamagata Prefecture in this simulation. Thus, as expected from the PBL wind errors, the behavior of the plume in the 15-km simulation was unnatural. The results of the Lagrangian simulations were similar. The behavior of the plume in the Lagrangian 15-km simulation (Fig. G-4-3d) was completely different from that in the 3-km (Fig. G-4-3e) and 500-m (Fig. G-4-3f) Lagrangian simulations. Similar to the Eulerian simulations, the 3-km and 500-m grid Lagrangian simulations showed good agreement, and both successfully reproduced the blockage of the ^{137}Cs plume along the Naka-dori Valley. In addition, the 15-km Lagrangian (Fig. G-4-3d) and

Eulerian (Fig. G-4-3a) simulations showed very similar ^{137}Cs distributions, although the simulated concentrations were quantitatively different.

In both the 15-km transport model results (Fig. G-4-4a and G-4-4d) for the total one-day accumulated deposition of ^{137}Cs on 15 March 2011 UTC, a highly polluted area extended broadly beyond Mt. Azuma and other mountains, across the Naka-dori Valley, and as far as Yamagata and Niigata prefectures. This distribution is similar to the surface concentration distribution (Fig. G-4-3a and G-4-3d). In addition, the most polluted area was not located near FDNPP but in the vicinity of the inland border between Fukushima and Yamagata prefectures. This unrealistic distribution was caused by wet deposition of the ^{137}Cs -137 plume after it passed the mountains beyond the Naka-dori Valley and extended into a heavy precipitation area. Such hot-spot pollution was not detected by the JAEA aerial observations. In contrast, both the 3-km (Fig. G-4-4b and G-4-4e) and 500-m (Fig. G-4-4c and G-4-4f) models showed that the heavily polluted area was mostly limited to eastern Fukushima Prefecture near FDNPP, consistent with the JAEA aerial observations.

G-4-4. Conclusion

A large difference was found in the PBL wind field between the 15-km resolution meteorological analysis and the analyses with 3 km and 500 m resolutions. The 15-km analysis could not reproduce Fukushima's mountainous topography in detail. Consequently, it failed to depict the complex wind structure over mountains and valleys. This error in the wind field caused large differences in the radionuclide transport and deposition simulation. In the real world, the ^{137}Cs plume from FDNPP, after crossing over the Abukuma Mountains, was apparently mostly blocked by Mt. Azuma and other mountains along the Naka-dori Valley. However, the 15-km grid simulations could not represent this blockage of the plume, which spread out unnaturally across the Naka-dori Valley. In contrast, the 3-km and 500-m simulations successfully reproduced the ^{137}Cs plume blockage along the Naka-dori Valley, and the two simulations produced highly similar distributions of ^{137}Cs surface concentrations and deposition. The behaviors simulated by the Eulerian and Lagrangian models were the same qualitatively, but the two models yielded quantitatively different results even when they were driven by the same meteorological analysis. More detailed information about these simulations is available in Sekiyama et al. (2015).

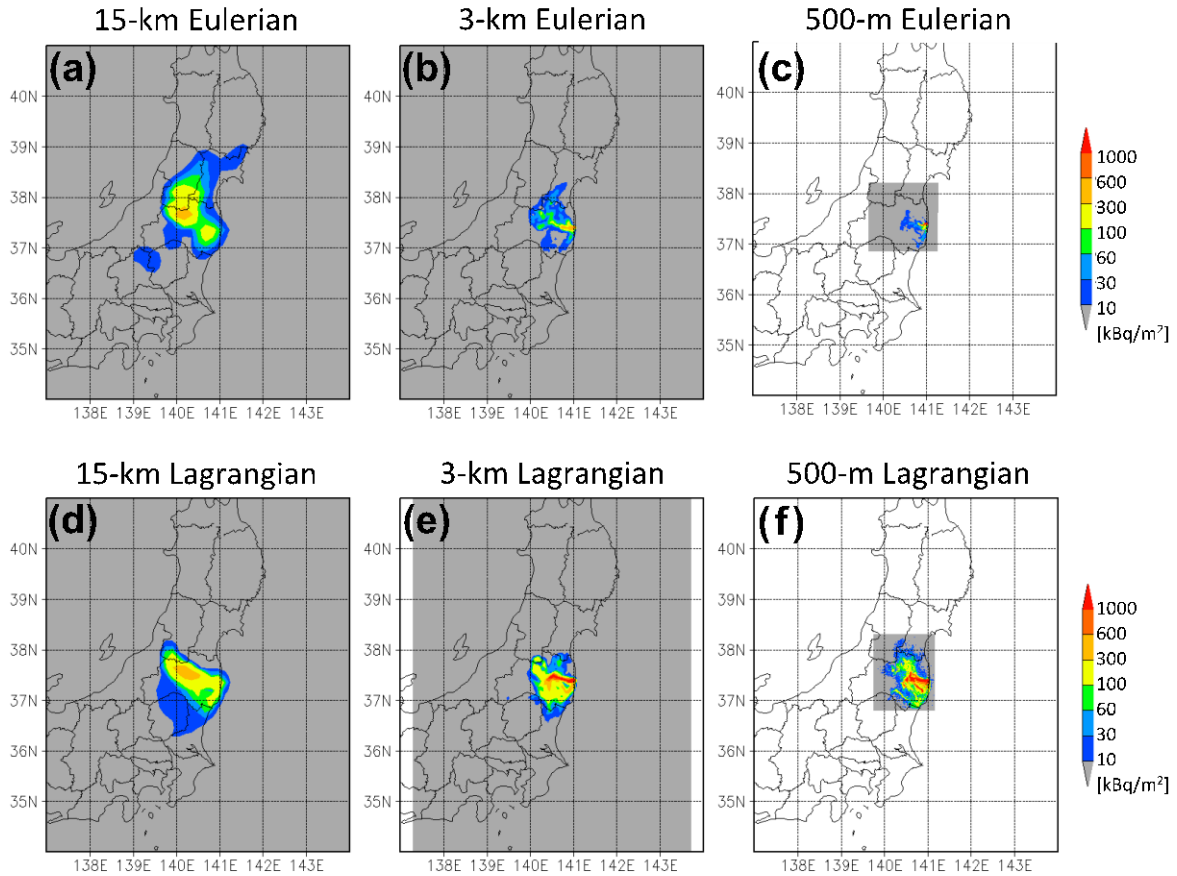


Fig. G-4-4. Total deposition of Cs-137 accumulated from 00:00 UTC 15 March to 00:00 UTC 16 March 2011 simulated by the Eulerian model RAQM2 with (a) 15-km grid meteorological analysis, (b) 3-km grid meteorological analysis, and (c) 500-m grid analysis. The same as simulated by the RAQM2, but simulated by the Lagrangian model JMA-RATM with (d) 15-km grid analysis, (e) 3-km grid analysis, and (f) 500-m grid analysis.

G-5. Emission source estimation by an inverse model¹

G-5-1. Introduction

Results of tracer transport simulations of radionuclides vary substantially depending on the source term conditions. Although more than four years have passed since the accident at the Fukushima Dai-ichi Nuclear Power Plant (FDNPP), robust source term estimates have still not been obtained.

Chino et al. (2011) and Terada et al. (2012) used a reverse method in which they compared radionuclide observational data with regional tracer transport model (SPEEDI) simulation results to obtain emission time series of ¹³⁷Cs and ¹³¹I. Chino et al. (2011) reported a preliminary estimate for the ¹³⁷Cs total emission amount from the FDNPP from 11 March to 6 April 2011 of 13.0 PBq and suggested that the maximum emissions occurred on 14 and 15 March. They also reported that large emission events occurred on 21–22 and 30–31 March. The Japan Atomic Energy Agency (JAEA) revised this estimate of the total release amount of ¹³⁷Cs for the period from 11 March to 19 April to 8.8 PBq (Terada et al., 2012). An important limitation of these analyses was that only data from Japanese land observation sites were used; therefore, they could not constrain radionuclide plumes transported over the Pacific Ocean.

Stohl et al. (2012) carried out a Bayesian synthesis inversion in which the results of a tagged global tracer transport model (FLEXPART) were used with observation data obtained mainly by the global radionuclide monitoring network operated by the preparatory commission for the Comprehensive Nuclear Test Ban Treaty Organization (CTBTO). They estimated the total ¹³⁷Cs emission amount from 11 March to 20 April to be 36.6 PBq, which is larger than the estimate reported by Terada et al. (2012) by a factor of 4. Their analysis included assessments of the radionuclide plumes that were transported over the Pacific Ocean because they used observation data from a wide area of the Northern Hemisphere and a global transport model. However, Stohl et al. (2012) used a Lagrangian transport model, which simulated the transport, diffusion, and deposition of large numbers of tracer particles released at the accident site. Although Lagrangian models are able to precisely calculate transport processes, they cannot estimate diffusion processes, such as turbulent, cumulus, and planetary boundary layer diffusion, or deposition processes (wet or dry) in detail, even though diffusion and deposition are the most important processes affecting the long-range transport of aerosol tracers. As a result, diffusion and deposition amounts might be affected.

In this section, we present a new estimate of the ¹³⁷Cs source term obtained by a Bayesian synthesis inversion method that coupled global observation network data with a global semi-Lagrangian aerosol transport model.

G-5-2. Analysis Method

The analysis method used tagged simulation results from the global semi-Lagrangian aerosol model MASINGAR (Tanaka and Chiba, 2005) with a TL319 horizontal resolution (approximately 60 km). Tagged tracers (¹³⁷Cs) from the lowest model layer (surface to 50 m) were released every 3 hours at a

¹ T. Maki

rate of 1 Tg/h. It was assumed that the released ^{137}Cs was attached to hydrophilic aerosols with an effective radius of 0.7 μm and was removed by dry and wet deposition. One of the merits of a tagged tracer simulation is that once ^{137}Cs source term emission time series are obtained, the ^{137}Cs atmospheric concentrations and depositions can be determined simply by calculating the linear combination of the source term estimations and the tagged tracer simulation results, without re-calculation of the aerosol model. As a result, we could construct a near-real-time prediction system by combining a properly distributed observation network and the operational tagged tracer transport model system (an emission prediction scenario is required when using such a system operationally). We used daily mean observation data of 51 global sites (CTBTO, Hoffmann et al., 2000; RING OF FIVE, Masson et al., 2011; University of California, Smith et al., 2014; Academia Sinica, Hsu et al., 2012; and Meteorological Research Institute, Igarashi et al., 2009) (Fig. G-5-1) and an analysis period of 40 days, from 11 March to 19 April. We tested two prior emission estimates. The first prior estimate was the JAEA posterior emission (Terada et al., 2012). For the second, we used the Norwegian Institute for Air Research prior emission (not posterior; Stohl et al., 2012) because our observational data were similar to theirs. The observational error, which included the spatial representation error, was set to 20%. The prior flux uncertainty is treated as a tuning parameter which shows the ratio between the observation and prior flux uncertainty, and several sensitivity tests were conducted by changing the prior emission flux uncertainties from 10% to 5000%.

G-5-3. Results and discussion

We selected the source term estimate of Stohl et al. (2012) as our prior emission estimate by comparing the mismatch between the observation data and the estimated concentrations. On the basis of the sensitivity test results, we set the prior flux uncertainty to 100%. The total ^{137}Cs emission amount from the FDNPP for the period from 11 March to 19 April was 19.4 PBq, and the estimated uncertainty was 3.0 PBq. In the present inverse analysis, the emission height level had only a small effect on the estimated time series of the source term. The maximum ^{137}Cs emission, which occurred on 15 March, was larger than the prior estimate emission estimate. Our results suggest that emission events occurred during 18–22 March and 28–30 March (Fig. G-5-2); however, the emission amount during 28–30 March was smaller than the estimates of Chino et al. (2011) and Terada et al. (2012).

In our analysis, which used tagged tracer simulation results, global observation data, and an inverse model, we obtained a total flux that was intermediate between the fluxes estimated by Stohl et al. (2012) and Terada et al. (2012) and consistent with other analysis results (Table G-5-1). We evaluated the atmospheric ^{137}Cs concentrations and deposition amounts by combining our estimate of total flux with the tagged simulation results.

However, to evaluate the results of our analysis several issues need to be addressed. One of the most important is that we used only one model, and the bias of the model transport could directly affect the estimated source term. For robust source term estimation, we should compile tagged model simulation results obtained with multiple models using the same experimental settings and compare their estimated

source terms. Another issue is the relatively coarse horizontal resolution of the model. To obtain a finer horizontal and temporal resolution, we should use a regional chemical transport model and collect hourly observation data. In addition, the available observation data for the Pacific Ocean are insufficient; therefore, to improve the analysis we should make use of marine deposition observation data.

Obsevation Points of Cs-137 ;Fukushima–Daiichi nuclear disaster.

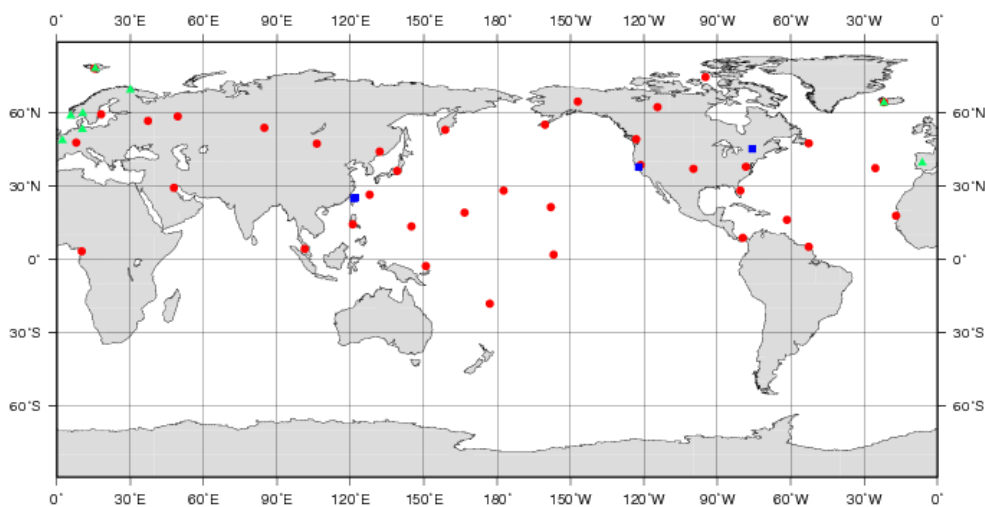


Fig. G-5-1. Locations of the observation data collection sites used in this study. Red, green, and blue circles show CTBTO, RING OF FIVE, and other observation sites, respectively.

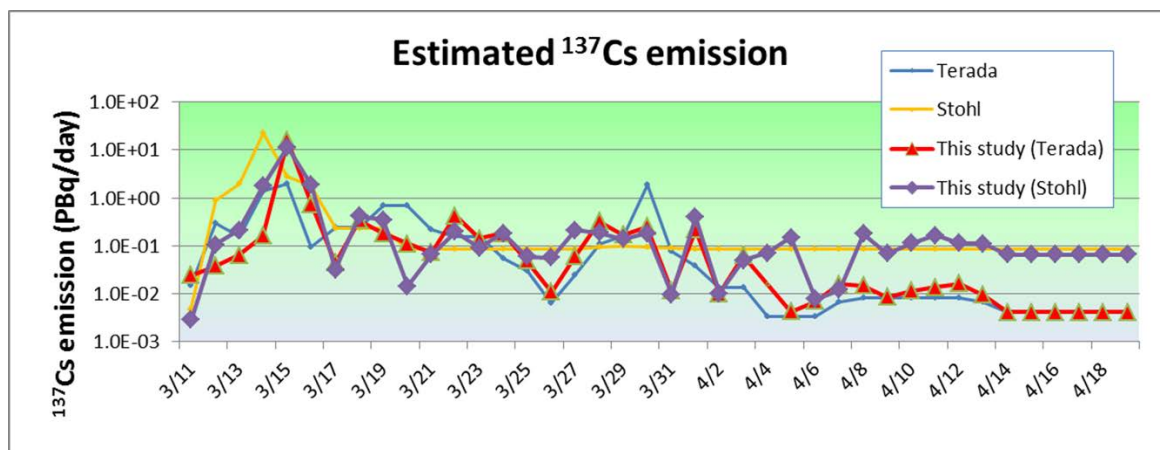


Fig. G-5-2. Estimated time series of ^{137}Cs emission from the FDNPP. The blue and orange lines show the source term time series obtained by Terada et al. (2012) and Stohl et al. (2012), respectively. The thick red and thick purple lines show the inversed posterior ^{137}Cs emission time series obtained by using emissions data of Terada and Stohl, respectively, as our prior emission estimate.

Table G-5-1. Recent ^{137}Cs source term estimations for the FDNPP accident.

Author	Total Flux	Remarks
This study	19.4 PBq (± 3.0 PBq)	(11 March–19 April)
IAEA (Terada et al., 2012)	8.8 PBq	(10 March–19 April)
Stohl et al. (2012)	36.6 PBq (207–537)	(10 March–20 April)
Winiarek et al. (2014)	10–15 PBq	(11 March–26 March)
MEXT (2011d) and Chino et al. (2011)	14–17 PBq	From obs. and numerical model analysis
MELCOR analysis (Gauntt et al. (2001))	16 PBq	From Stohl et al. (2012)
IRSN (Institut de radioprotection et de sûreté nucléaire)	30 PBq	From Stohl et al. (2012)
ZAMG (Zentralanstalt für Meteorologie und Geodynamik)	67 PBq	From Stohl et al. (2012)

G-6. Science Council of Japan atmospheric transport model intercomparison¹

G-6-1. Introduction

In this section, we describe the model intercomparison project of the Science Council of Japan (SCJ) and the contributions of the Meteorological Research Institute (MRI) to the intercomparison. SCJ launched a working group for model intercomparison under the Subcommittee of Investigation on the Environmental Contamination Caused by the Nuclear Accident in the Sectional Committee on Nuclear Accident, Committee on Comprehensive Synthetic Engineering, in July 2012. The objective of the SCJ working group was to assess the uncertainties in the results of experiments simulating the transport of radioactive materials from the Fukushima Daiichi Nuclear Power Plant accident by comparing existing model results.

The chair of the working group, Prof. Teruyuki Nakajima of the University of Tokyo, invited individuals from several research institutions and universities who had conducted research on the transport of radionuclides to be members. In October 2012, the working group issued a call for participation in the SCJ intercomparison, including to the World Meteorological Organization (WMO) Task Team. The members of the Task Team discussed the matter and decided that the Task Team would not participate as a whole team, but that the decision as to whether to participate would be left to individual members. Following this decision, the Japan Meteorological Agency (JMA) chose to participate; thus, JMA's Task Team and researchers in MRI participated in the SCJ intercomparison.

G-6-2. Brief description of the model intercomparison

The SCJ model intercomparison consisted of four parts: regional atmospheric transport, global-scale atmospheric transport, oceanic transport of radionuclides, and emission source estimation by inversion methods. The contributing groups were asked to provide their best simulation results as of spring 2013. Because the objective of the intercomparison was to evaluate the characteristics and accuracies of the currently available simulated results, uniform conditions were not imposed. Therefore, there were large differences in model setup (e.g., grid resolution and integration time interval) and the data (meteorological field data and emission scenarios) used to constrain each simulation. However, this no-constraint policy made it difficult to investigate the causes of the differences in the simulation results.

In total, 9 regional atmospheric models, 6 global atmospheric models, and 11 oceanic models were included in the SCJ model intercomparison. In this section, the contributions of JMA to the intercomparison of regional and global-scale atmospheric transport models are presented. JMA also contributed to the SCJ intercomparison by using an inverse model to estimate the emission flux by an inversion method; these results are described in section G-5 of this technical report.

¹ T.Y. Tanaka

G-6-3. Regional atmospheric transport model intercomparison

For the regional atmospheric transport intercomparison, nine contributing groups provided nine sets of simulated results (Takigawa et al., 2013). The contributing groups were the Centre d'Enseignement et de Recherche en Environnement Atmosphérique (Winiarek et al., 2014), the Central Research Institute of Electric Power Industry (Hayami et al., 2012), the Institut de radioprotection et de sûreté nucléaire (Korsakissok et al., 2013), the Japan Atomic Energy Agency (JAEA) (Terada et al., 2008), the Japan Agency for Marine-Earth Science and Technology (JAMSTEC), JMA (Saito et al., 2014), MRI (Kajino et al., 2012a, 2012b; Adachi et al., 2013; Sekiyama et al., 2015), the National Institute for Environmental Studies (Morino et al., 2011, 2013), and Seoul National University (Park et al., 2013).

MRI contributed results obtained with the regional chemistry transport models NHM-Chem (Kajino et al., 2012a, 2012b; Sekiyama et al., 2013, 2015) and JMA-RATM (Saito et al., 2014) to the intercomparison of regional transport. Detailed descriptions of NHM-Chem and its results are given in sections G-3 and G-4 of this technical report. The version of JMA-RATM used for the SCJ regional atmospheric model intercomparison was slightly modified from the WMO Task Team version. The main differences were (1) the radionuclide emission scenario was changed to “JAEA2” (Kobayashi et al., 2013), (2) the time step of the integration was shortened to 5 minutes, and (3) snow and hail as well as rain from the meso-analysis of accumulated precipitation were used. JMA-RATM and its results are described in detail in section E of this technical report. The horizontal distribution of the accumulated ^{137}Cs deposition during March 2011 simulated by JMA-RATM is shown in Fig. G-6-1a.

The regional atmospheric model intercomparison results showed that the land area deposition was $27 \pm 10\%$ of total emissions. However, MEXT aircraft observations on 31 May 2012 showed on-land deposition to be 2.7 PBq (Torii et al., 2012). This observed value and the total emissions estimated by inverse analysis (17.8 ± 8.9 PBq; section G-5) lead to a land area deposition of $18 \pm 7\%$ of total emissions, but to a value of $20 \pm 6\%$ if a total emission of 14.6 ± 3.5 PBq, which is within two standard deviations of the mean, is used. These differences in the land area deposition percentage are due to model simulation errors, and errors in the total emission estimate and in the estimate of the land-deposited amount from aircraft observations.

G-6-4. Global atmospheric transport model intercomparison

The intercomparison of global-scale transport models included 5 global transport models, 1 large-scale regional transport model, and 12 simulated results. Four of the five global models, SPRINTARS (Takemura et al., 2011), EMAC (Christoudias and Lelieveld, 2013), Model of Aerosol Species IN the Global Atmosphere (MASINGAR)-1 (Tanaka et al., 2003), and MASINGAR mk-2 (Tanaka et al., 2012), are global aerosol models that are coupled online with general circulation models. The remaining models are the TM5 global transport model (Huijnen et al., 2010) and the MRI Passive-tracers Model for radionuclides (MRI-PM/r) regional transport model (Kajino et al., 2012a, 2012b; Adachi et al., 2013), which are off-line models that use assimilated meteorological fields or meteorological fields previously calculated by another model. All of the participating models in the SCJ intercomparison were grid point

Eulerian or semi-Lagrangian advection models.

MRI contributed three models to the global atmospheric transport model intercomparison: MASINGAR-1 (Tanaka et al., 2003), MASINGAR mk-2 (Tanaka et al., 2012) and MRI-PM/r. The simulated results of two versions of MASINGAR were submitted for the intercomparison. MASINGAR-1 was coupled with an atmospheric general circulation model (AGCM) called MRI/JMA 98, which has been used as JMA's operational dust forecasting model since January 2004 (Tanaka et al., 2003). The model resolutions were set to a T106 Gaussian horizontal grid (approximately $1.125^\circ \times 1.125^\circ$) and 30 vertical layers from the surface to a height of 0.4 hPa. A newer version of this aerosol model, called MASINGAR mk-2, was coupled with an AGCM called MRI-AGCM3, which is a component of MRI's earth system model MRI-ESM1 (Yukimoto et al., 2011, 2012). MASINGAR mk-2 was also used as the global aerosol model for the CMIP5 climate change experiment. For the intercomparison, the model resolutions were set to a TL319 horizontal grid (approximately $0.5625^\circ \times 0.5625^\circ$) and 40 vertical layers from the ground surface to a height of 0.4 hPa. In this intercomparison experiment, the horizontal wind fields were assimilated from six-hourly $1.25^\circ \times 1.25^\circ$ JMA Climate Data Assimilation System (JCDAS) global reanalysis data (Onogi et al., 2007) using a Newtonian relaxation nudging technique. The JCDAS reanalysis was also used for sea-surface temperature data. The released ^{137}Cs was assumed to be readily attached to ambient aerosols with a unimodal lognormal distribution (mode radius, $0.07 \mu\text{m}$; dispersion, 2.0) (Tanaka et al., 2012). For the intercomparison, the ^{137}Cs results simulated with the source terms of JAEA (Terada et al. 2012) and Stohl et al. (2012) were submitted. For the ^{133}Xe experiment, the inversely estimated source term of Stohl et al. (2012) was used.

MRI-PM/r is a large-scale regional off-line chemistry transport model. The regional domain used was 107°E – 252°E and 3°N – 61°N with 234×120 grids (Mercator map projection), which corresponded to a horizontal resolution of approximately $60 \text{ km} \times 60 \text{ km}$. The vertical coordinates were terrain-following with 13 vertical layers up to 10 hPa. The Advanced Research Weather Research and Forecasting model (WRF; Skamarock et al., 2008) was used to simulate the meteorological field. The U.S. National Centers for Environmental Prediction six-hourly, $1^\circ \times 1^\circ$ final operational global analysis dataset ds083.2 (<http://rda.ucar.edu/datasets/ds083.2/>) was used for the initial and boundary conditions of WRF and also for the analysis nudging method. The aerosol module used a category approach to represent the interaction between radionuclides and environmental species (Kajino and Kondo, 2011). The aerosol particles were grouped into six categories: primary hot particles (PRI), Aitken mode (ATK), accumulation mode (ACM), dust particles (DU), sea-salt particles (SS), and pollen (POL). The aerosol chemical and dynamical processes, such as nucleation, condensation, coagulation and deposition, were calculated by a modal moment dynamics approach (Kajino and Kondo, 2011; Kajino, 2011; Kajino et al. 2012a, 2012b). The emission inventory of environmental species with anthropogenic, biogenic, and biomass burning origins was the same as that used by Kajino and Kondo (2011). Five percent of the Cs was assumed to form radioactive primary particles (PRI), and the remaining 95% was assumed to condense onto pre-existing particles of the other five types with the mass fluxes proportional to the

surface area concentrations of each aerosol category. A revised version of the JAEA inventory (Terada et al., 2012) was used for the emissions of ^{134}Cs and ^{137}Cs .

The simulated horizontal distributions of the accumulated ^{137}Cs deposition through the end of March 2011 obtained with the MRI global-scale models are shown in Fig. G-6-1b–f. All of the simulated results show the ^{137}Cs deposited over a wide area of the Northern Hemisphere, with the highest concentrations in the Northwest Pacific region. The global-scale model intercomparison results indicate that the global wet deposition accounted for $93 \pm 5\%$ of the total ^{137}Cs deposition. The JMA-RATM results (Fig. G-6-1a), however, showed that 46% of ^{137}Cs was removed by wet deposition in the simulation region, and the regional atmospheric model intercomparison results showed that $68 \pm 20\%$ of ^{137}Cs was removed by wet deposition over the simulation regions. The cause of these differences between the global and regional simulations was mainly the different simulation regions, because dry deposition was dominant in the vicinity of the power plant where concentrations of ^{137}Cs were high. However, another non-negligible cause was differences among the models in the treatment of dry and wet deposition and in the meteorological fields used.

G-6-5. Summary

The SCJ intercomparison of regional and global atmospheric transport model simulation results showed that the models were capable of depicting the main features of the observed radioactive material distributions. Quantitative comparisons of the simulation results, however, revealed large uncertainties, especially in the amount of wet deposition. The skill of the models depends on the performance of the dynamic frameworks, chemical transportation processes, dry and wet deposition processes and other elements. Therefore, the models can be significantly improved through collaboration among the different modeling communities. The full report of the SCJ model intercomparison project was published by the Sectional Committee on Nuclear Accident, Committee on Comprehensive Synthetic Engineering, of SCJ on 2 September 2014 (SCJ, 2014).

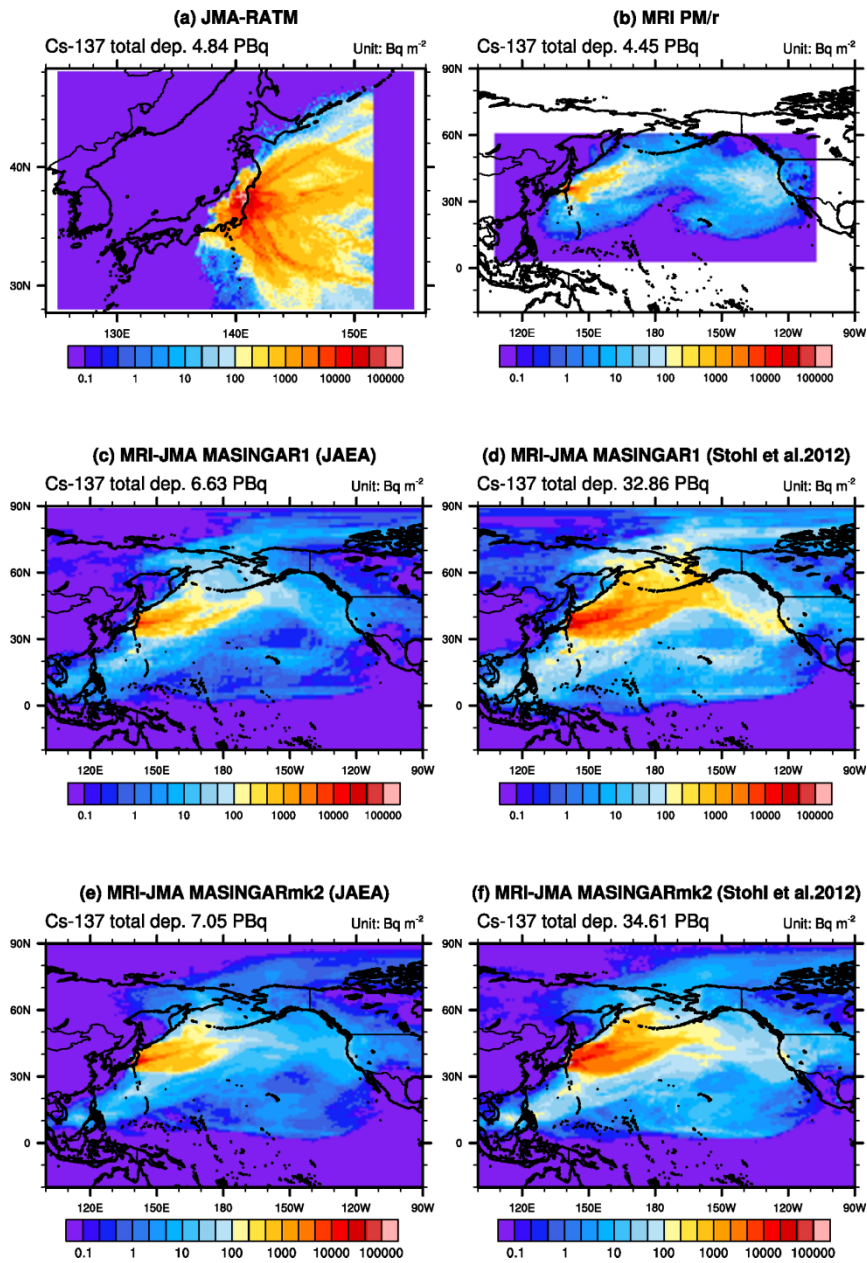


Fig. G-6-1. Horizontal distributions of the accumulated ¹³⁷Cs deposition from 11 to 31 March 2011 by (a) JMA-RATM, (b) NHM-Chem, (c) MASINGAR-1 using the JAEA source term, (d) MASINGAR-1 using the Stohl et al. (2012) source term, (e) MASINGAR mk-2 using the JAEA source term, and (f) MASINGAR mk-2 using the Stohl et al. (2012) source term. Units are Bq m⁻².